Original Research

ZnO/RGO Nanocomposites Incorporating Green-Electrochemically Synthesized RGO for Sonocatalytic Dye Degradation

Ahmed Mostafa[1], **M.A. Ibrahim**[1], **Hesham A. Yousef** [1], **A. Ashour**[2,*]

[1] Physics Department, Faculty of Science, Suez University, P.O. Box: 43221, Suez, Egypt.

[2] Physics Department, Faculty of Science, Islamic University of Madinah, Madinah 42351, Saudi Arabia.

* Correspondence: aashour_2000@iu.edu.sa

Received: November 19, 2025; Accepted: February 24, 2026

Abstract: In this study, zinc oxide nanoparticles (ZnO NPs), reduced graphene oxide (RGO) nanosheets (NShs), and their hybrid ZnO/RGO nanocomposites (NCs) were synthesized using environmentally benign and sustainable routes. The prepared materials were systematically characterized and evaluated for their sonocatalytic performance toward methylene blue (MB) degradation. Structural and morphological analyses confirmed the formation of highly crystalline ZnO and the successful integration of RGO within the composite matrix. SEM observations revealed that ZnO NPs with sizes ranging from approximately 30 to 60 nm were uniformly anchored onto the folded and wrinkled surfaces of RGO NShs. Elemental purity was verified by EDX analysis, while FTIR and TGA results evidenced strong interfacial interactions and enhanced thermal stability in the ZnO/RGO NCs. Sonocatalytic experiments demonstrated a pronounced enhancement in MB degradation upon RGO incorporation. While pristine ZnO achieved only ~50% MB removal within 60 min, the ZnO/20% RGO NC exhibited superior activity, achieving over 90% degradation under identical conditions. Kinetic analysis revealed a substantial increase in the apparent rate constant, with ZnO/20% RGO showing the highest value ($k = 0.051\ min^{-1}$), nearly three times that of pure ZnO ($k = 0.018\ min^{-1}$). Correspondingly, the MB half-life was significantly reduced from 38.5 min for ZnO to 13.6 min for ZnO/20% RGO NC. The enhanced sonocatalytic performance is attributed to the synergistic effects of ultrasonic cavitation and the ZnO/RGO heterointerface, which promotes efficient charge separation, accelerates electron transport, and enhances reactive oxygen species generation. Reusability tests confirmed excellent stability, with ZnO/20% RGO NC retaining more than 95% of its initial efficiency after five consecutive cycles, whereas pristine ZnO suffered rapid deactivation. These results demonstrate that ZnO/RGO NCs with optimized RGO loading, particularly at 20%, represent robust, efficient, and sustainable sonocatalysts for wastewater remediation applications.

Keywords: ZnO NPs; RGO NShs; ZnO/RGO NCs Characteristics; Sonocatalytic Degradation; MB.

1. Introduction

The rapid expansion of industrial and manufacturing activities over recent decades has led to the large-scale discharge of synthetic dyes into aquatic environments, with MB being among the most frequently detected contaminants. Owing to their complex aromatic structures, high chemical stability, and pronounced resistance to biodegradation, such dyes are poorly removed by conventional wastewater treatment methods, including biological oxidation, adsorption, and coagulation processes. As a result, persistent dye residues continue to accumulate in water bodies, posing serious risks to aquatic ecosystems and human health even at low concentrations [1–4].

In response to these challenges, advanced oxidation processes (AOPs) have attracted considerable attention as effective strategies for the degradation of recalcitrant organic pollutants

through the in situ generation of highly reactive species, particularly hydroxyl radicals. Among various AOPs, semiconductor-based catalytic processes have emerged as promising approaches due to their relatively simple operation, chemical stability, and environmental compatibility [5–7]. ZnO is one of the most extensively investigated semiconductor catalysts because of its low cost, natural abundance, non-toxicity, and strong redox capability. Numerous studies have reported ZnO-based catalysts achieving MB degradation efficiencies of 40–70% within 60–120 min under different activation modes [6,8,9,10]. However, the practical application of ZnO remains limited by intrinsic drawbacks, most notably the rapid recombination of photogenerated charge carriers and its reduced efficiency under visible-light or non-photonic activation conditions [11–15]. These limitations significantly suppress catalytic activity and hinder large-scale deployment.

To overcome these challenges, ZnO-based hybrid NCs incorporating carbonaceous materials have been widely explored. RGO NShs, in particular, has received significant attention due to its high electrical conductivity, large specific surface area, and excellent electron-accepting capability [12,14,6,17], which collectively promote charge separation and suppress electron–hole recombination [11,18]. Previous studies on ZnO/RGO systems have reported improved MB degradation efficiencies exceeding 80% and apparent rate constants in the range of 0.02–0.04 min^{-1}, depending on synthesis method and operating conditions [16,19,20,21]. Despite these advances, many reports rely on a fixed or arbitrarily selected RGO content, with limited systematic investigation of how RGO loading quantitatively influences catalytic efficiency, reaction kinetics, and charge-transfer dynamics [22–26]. Furthermore, catalyst stability and recyclability are often assessed only qualitatively or over a small number of cycles, preventing a rigorous evaluation of long-term performance and practical applicability.

In parallel with material development, sonocatalysis—where catalytic reactions are enhanced by ultrasonic irradiation—has emerged as an effective alternative activation strategy for pollutant degradation. Ultrasonic irradiation induces acoustic cavitation, generating localized hot spots with extreme temperatures and pressures, enhancing mass transfer, and facilitating the formation of reactive oxygen species such as hydroxyl radicals [23,27]. Recent studies have demonstrated that sonocatalytic systems can achieve faster degradation kinetics than conventional photocatalytic processes, particularly in turbid or light-limited environments [24,28,29,30]. However, the synergistic interaction between ZnO/RGO NCs and ultrasonic activation remains insufficiently understood. In particular, composition-dependent sonocatalytic performance, kinetic enhancement mechanisms, and catalyst durability under prolonged ultrasonic exposure have not been systematically addressed.

Against this background, the present study aims to bridge these gaps by synthesizing ZnO NPs, RGO NShs, and ZnO/RGO NCs with systematically varied RGO loadings. The structural, morphological, compositional, and thermal properties of the prepared materials are comprehensively characterized, and their sonocatalytic performance toward MB degradation is quantitatively evaluated. Special emphasis is placed on elucidating the role of RGO content in governing degradation efficiency, kinetic behavior, and long-term stability under ultrasonic irradiation. By providing a detailed composition–performance relationship, this work offers a clearer framework for the rational design of efficient and durable ZnO/RGO sonocatalysts for wastewater remediation applications.

2. Materials syntheses and experimental systems

2.1. Materials

All chemicals were of analytical grade and used as received. Graphite rods recovered from spent carbon batteries were employed as the working and counter electrodes. The graphite electrodes were purified prior to use. Hydrochloric acid (HCl, 37%, Merck), sulfuric acid (H_2SO_4, 98%, Merck; 0.5 M, 1.0 M, and 2.0 M aqueous solutions), acetone (≥99.5%, Merck), ethanol (≥99.5%, Merck), and distilled water were used for electrode purification and electrochemical processing.

Zinc acetate dihydrate ($Zn(CH_3COO)_2 \cdot 2H_2O$, ≥99%, Sigma-Aldrich) was used as the zinc precursor. Sodium hydroxide (NaOH, ≥98%, Merck) was used as the precipitating agent. Ethanol and distilled water were used as solvents.

2.1.1. Synthesis of ZnO NPs

A sol–gel method was employed for the synthesis of ZnO NPs. Zinc acetate dihydrate (0.1 mol) was dissolved in 100 mL of ethanol under continuous magnetic stirring at room temperature. The solution was subsequently heated to 50–60 °C and stirred for 30 min to ensure complete dissolution of the precursor. Separately, sodium hydroxide (0.2 mol) was dissolved in 100 mL of ethanol and stirred for 10–15 min until a clear solution was obtained. The NaOH solution was then added dropwise to the zinc acetate solution under constant stirring. During the addition process, the reaction temperature was maintained between 60 and 70 °C, as recommended in the literature [7,8,31]. The reaction mixture was continuously stirred for 1–2 h, during which the formation of a white precipitate was observed, indicating gelation. The pH of the mixture was maintained in the range of 9–11, noting that slight variations in pH during gelation and ZnO formation are expected. After gel formation, the sol was allowed to stand undisturbed at room temperature for 12–24 h to promote particle growth and stabilization. The resulting gel was separated from the supernatant by centrifugation or filtration, followed by repeated washing with ethanol and distilled water to remove residual ions and byproducts. The obtained solid was dried in an oven at 80–100 °C for 6–12 h to eliminate residual solvents and moisture. Finally, the dried powder was calcined in air at 400–500 °C for 2–3 h using a muffle furnace to achieve crystallization and remove organic residues. Figure 1 shows the process of ZnO NPs synthesis.

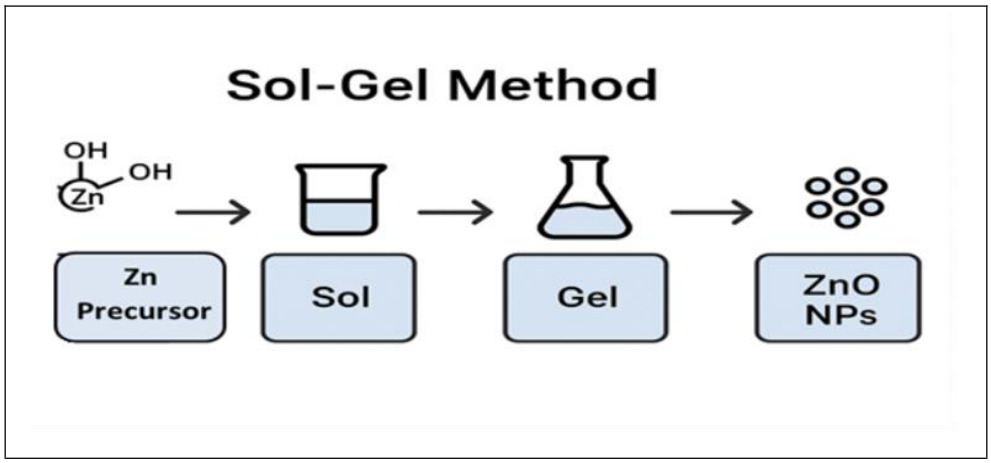

Figure 1. Facile synthesis of ZnO NPs using sol-gel method [8,31].

2.1.2. Green synthesis of RGO nanosheets using novel method

RGO NShs were synthesized via a novel green electrochemical exfoliation approach using waste-derived carbon materials as the precursor. Graphite rods were recovered from spent commercial batteries, thoroughly cleaned to remove residual electrolytes and surface impurities, and subsequently employed as carbon electrodes in the electrochemical cell. This strategy not only lowers material costs but also promotes the valorization of carbonaceous waste, thereby contributing to environmental sustainability [13,32,33]. Electrochemical exfoliation was performed in an aqueous H_2SO_4 electrolyte with a controlled concentration. Two graphite electrodes—waste-derived graphite serving as the working electrode and a graphite rod as the counter electrode—were positioned parallel to each other and connected to a regulated direct-current power supply operating at 12 V. Upon voltage application, anodic exfoliation of graphite occurred, resulting in the progressive delamination of graphene-based NShs into the

electrolyte. After completion of the exfoliation process, the resulting suspension was collected, repeatedly washed with distilled water until a neutral pH was attained, and then filtered [33–35]. The obtained product was dried at a moderate temperature to yield RGO NShs. Compared with conventional chemical oxidation–reduction routes; this electrochemical method eliminates the use of toxic oxidizing agents and chemical reducing reagents, significantly minimizes chemical waste, and exploits waste-derived carbon feedstock, rendering it a greener and more sustainable pathway for RGO production, as illustrated in Figure 2.

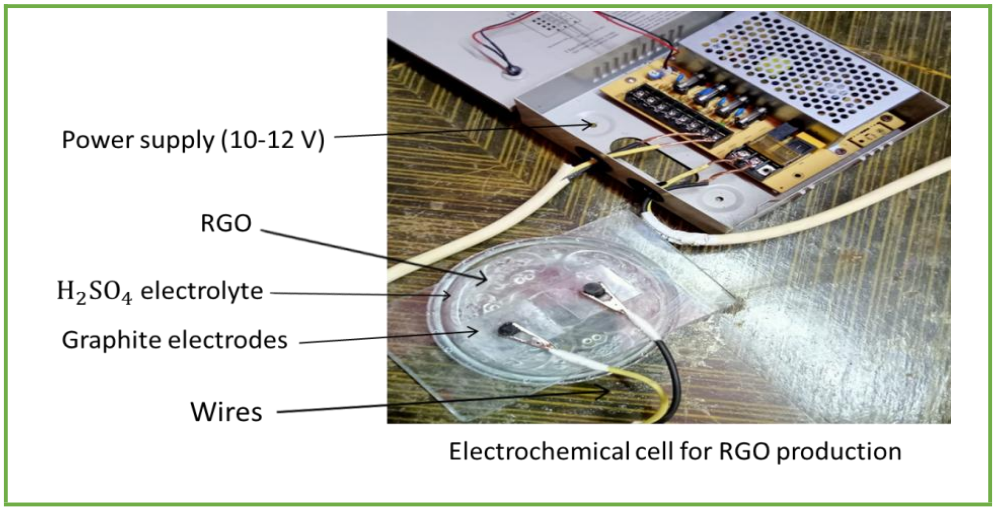

Figure 2. An electrochemical cell for RGO production using green novel method.

2.1.3. Synthesis of ZnO/RGO NCs

ZnO/RGO NCs were prepared using an ultrasonic-assisted solution method. Initially, 1.0 g of RGO was dispersed in 150 mL of deionized water and ultrasonicated for 30 min to achieve uniform dispersion and partial exfoliation of the RGO sheets. In a separate step, 0.25 g of ZnO NPs was dispersed in 50 mL of distilled water and ultrasonicated for the same duration [17,36].The two suspensions were subsequently combined and further ultrasonicated for 45 min to promote homogeneous interaction and intimate contact between ZnO NPs and RGO NShs. After sonication, the resulting mixture was stirred continuously for 1 h to enhance composite formation. The final suspension was dried in a hot-air oven until complete removal of solvent. The obtained dried powders correspond to ZnO/RGO NCs with RGO loadings of 5, 10, 15, 20, and 25 wt%, as schematically illustrated in Figure 3.

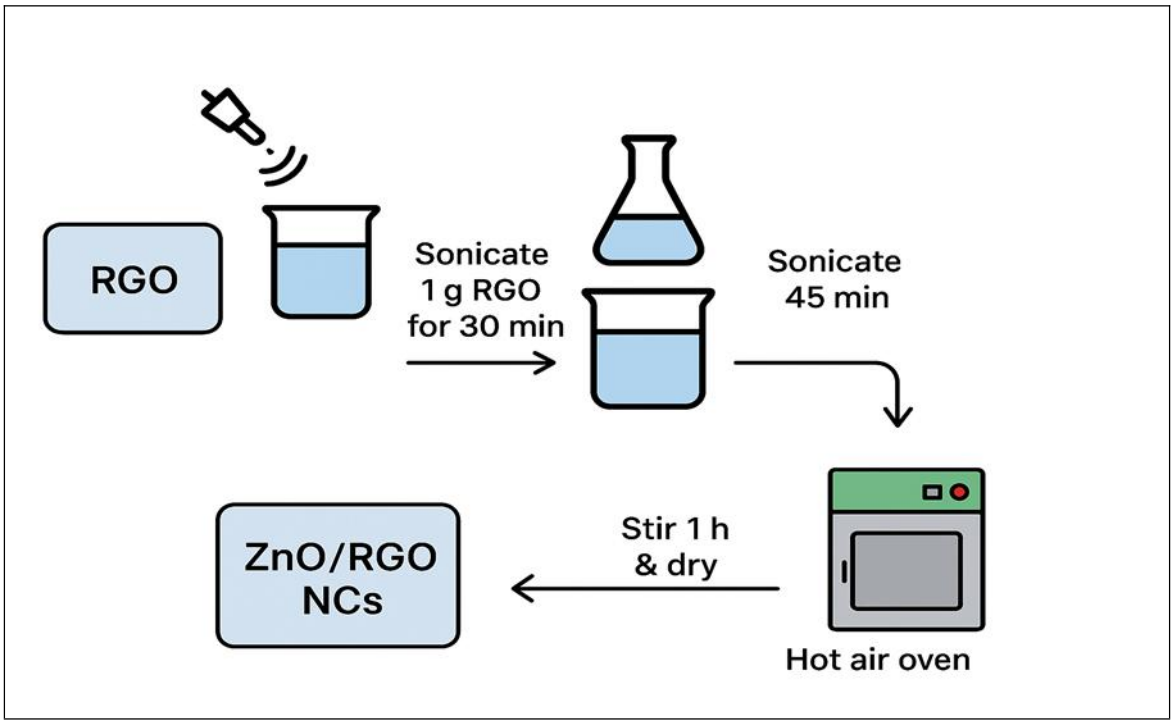

Figure 3. Simple synthesis of ZnO/RGO NCs [37].

2.2. Experimental systems

2.2.1. XRD system

XRD analyses were performed at the Central Laboratory of El-Minia University using a JEOL diffractometer (Model 60PA-JSDX) operating at 42 × 10^3 V and 36 × 10^{-3} A. The instrument was equipped with a Cu Kα radiation source (λ = 1.54184 Å) and operated at a scan rate of 1° min^{-1} with a time constant of 1 s. Diffraction patterns were recorded within the 2θ range of 30°–90°, providing reliable phase identification and crystallographic orientation [38]. The acquired data were further analyzed to extract microstructural parameters using the Rietveld refinement method implemented in the MAUD software, supported by additional computational tools such as X'Pert HighScore Plus software where necessary [18,39].

2.2.2. SEM and EDX systems

The morphology and size characteristics of the prepared nanomaterials were evaluated using a set of advanced electron microscopy tools. Surface topography of the bulk specimens was analyzed with a JEOL scanning electron microscope (JSM- IT200) operated at an accelerating voltage of 25 kV [41]. To obtain detailed information on particle shape, dimensions, and internal structure, high-resolution transmission electron microscopy (HRTEM, JEOL 3010, Japan) was carried out at 200 kV for both ZnO NPs and ZnO/RGO NCs. Additional observations relating to particle distribution, surface features, and elemental composition were obtained using a ZEISS EVO-MA10 SEM equipped with an energy-dispersive X-ray (EDX) detector [42]. SEM images were processed using ImageJ software to determine particle size distributions based on statistical analysis of more than 100 particles per sample, while elemental composition obtained from EDX was evaluated using the instrument-integrated EDX analysis software [29,43].

2.2.3. FTIR system

FTIR spectroscopy was carried out in transmission mode using a Spectrum One spectrometer (PerkinElmer) over the range of 4000–400 cm^{-1} with a spectral resolution of 4 cm^{-1}, averaged over 20 scans. The samples were prepared by dilution with KBr at a ratio of 2:300 (sample:KBr) and

analyzed using KBr pellets, with a pure pellet serving as the reference [44]. FTIR spectra were analyzed using OMNIC software to identify functional groups and bonding characteristics.

2.2.4. TGA system

Thermogravimetric analysis (TGA) was carried out to examine how the samples respond to heating and to monitor their stepwise mass loss. Differential thermal analysis (DTA) complemented these measurements by revealing the corresponding thermal events occurring during decomposition. The thermal behavior of the ZnO NPs and the ZnO/RGO NCs was assessed using a Q50 thermogravimetric analyzer (TA Instruments, USA). For each run, about 10 mg of material was placed in the furnace and heated from 35 to 1000 °C at a rate of 10 °C min^{-1} under a flowing nitrogen atmosphere, following the procedure described in reference [45–47]. TGA data were processed using TA Universal Analysis software to evaluate thermal stability and compositional changes.

2.2.5. Kinetic analysis of MB degradation under sonicated and non-sonicated conditions

MB was selected as the model organic dye to evaluate the photocatalytic performance of ZnO/RGO NCs. A stock solution of MB (10 mg L^{-1}) was prepared using deionized water and diluted as required to obtain the working concentration. All experiments were performed with a solution volume of 100 mL under ambient atmospheric conditions. The absorbance of MB was correlated to its concentration according to the Beer–Lambert law, with a proportionality constant of 0.1 absorbance units per mg L^{-1}. The catalytic reactions were conducted by dispersing the prepared soncatalyst in the MB solution at a dosage of 0.5 g L^{-1} [48].

For ultrasonic-assisted studies, the reaction mixture was subjected to sonication using an ultrasonic bath operating at a fixed frequency of 40 kHz and a power of 200 W. The temperature of the solution was maintained at 25 ± 2 °C using a circulating water bath to avoid thermal effects during the process. In control experiments (without sonication), the same catalyst concentration and environmental conditions were applied to ensure a direct comparison of degradation efficiency. The temporal evolution of MB concentration was monitored using UV-2600 spectrophotometer from Shimadzu at the national research center in Cairo, recording absorbance spectra in the range of 500–800 nm [49]. The characteristic absorption maxima of MB at approximately 610 nm and 665 nm were used as references to quantify dye concentration. Aliquots of the reaction mixture were collected at predetermined intervals (0–90 min, with a 4 min step), centrifuged to remove suspended catalyst particles, and subsequently analyzed for residual MB concentration.

The degradation efficiency of MB was calculated using Eq. (1) [23]:

$$\text{Degradation (D\%)} = \frac{C_0 - C_t}{C_0} \times 100 \quad (1)$$

where C_0 and C_t represent the initial and time-dependent dye concentrations, respectively.

The degradation behavior of MB was found to follow pseudo-first-order kinetics, described by Eq. (2) [16]:

$$\ln\left(\frac{C_0}{C_t}\right) = kt \quad (2)$$

The rate constant k (min^{-1}) was obtained from the slope of the linear plot of $\ln(C_0/C_t)$ versus time, allowing a direct comparison of the reaction rates under sonicated and non-sonicated conditions. MB degradation under sonicated and non-sonicated conditions was performed using OriginPro software, where absorbance data were converted to concentration values based on the Beer–Lambert law, and apparent rate constants were obtained from pseudo-first-order kinetic fitting [27].

2.2.6. Statistical analysis and reproducibility

All quantitative experiments in this study were conducted under strictly controlled and reproducible conditions, following established statistical validation protocols. Sonocatalytic degradation experiments of MB, kinetic analyses, recyclability assessments, and particle size measurements were each performed in triplicate (n = 3) under identical experimental conditions to ensure data reliability and experimental consistency. Experimental data are presented as mean values ± standard deviation (SD). Statistical variability was evaluated using the relative standard deviation (RSD), defined as the ratio of the standard deviation to the corresponding mean value and expressed as a percentage. For all sonocatalytic performance parameters—including degradation efficiency, apparent pseudo-first-order rate constants, initial reaction rates, and half-life values—the RSD values remained below 5%, indicating excellent reproducibility and high experimental stability. Error bars representing ± SD are included in all relevant figures (Figures 14–20) to clearly illustrate data dispersion and reproducibility. Particle size distributions were determined from SEM micrographs by measuring more than 100 individual particles per sample using ImageJ software, and the corresponding mean particle sizes and standard deviations were calculated accordingly. Kinetic analysis of MB degradation was carried out assuming a pseudo-first-order reaction model, with apparent rate constants (k) obtained through linear regression fitting. All kinetic calculations, statistical averaging, regression analyses, and graphical representations were performed using OriginPro software. Recyclability and stability tests were conducted over five consecutive catalytic cycles, with each cycle independently repeated three times. The consistent degradation efficiencies and low RSD values observed across successive cycles further demonstrate the robustness, durability, and statistical reliability of the synthesized ZnO/RGO NCs.

3. Results and discussions

3.1. Structural integrity and phase purity of ZnO/RGO NCs

XRD confirmed the structural integrity and crystallinity of the synthesized materials. Graphite exhibited a sharp peak at 2θ = 26.38°, while RGO showed a broadened peak at 23.18°, reflecting exfoliation, partial reduction, and increased interlayer spacing. ZnO NPs presented well-defined reflections indexed to the hexagonal wurtzite phase with no impurities, indicating high purity and crystallinity, with the (101) plane suggesting preferential growth. In ZnO/RGO NCs, both ZnO and RGO peaks were preserved, confirming successful integration without structural disruption. Peak broadening and slight shifts with higher RGO loadings indicated lattice strain and defect formation, while enhanced peak intensities suggested improved crystallinity. Collectively, these results demonstrate the formation of crystalline RGO, pure ZnO, and stable ZnO/RGO hybrids with strong interfacial interactions that underpin their potential functional performance.

3.1.1. XRD of RGO NShs

The XRD patterns of graphite and RGO NShs are illustrated in Figure 4. Graphite exhibits a sharp and intense diffraction peak at 2θ = 26.38°, corresponding to the (002) plane, which is characteristic of a highly ordered graphitic structure. In contrast, the RGO NShs display a broad peak centered at 23.18°, indicating partial reduction of oxygen groups and the re-stacking of graphene layers with an expanded interlayer spacing. Additional peaks observed at 43.09° and 44.42° correspond to the (100) and (101) planes, respectively, reflecting the presence of residual graphitic domains. The broadening and shift of the peaks in the RGO pattern relative to graphite confirm successful exfoliation and structural modification, resulting in a more disordered and less crystalline framework. These findings emphasize the transformation from the ordered arrangement of graphite to the partially disordered structure of RGO NShs.

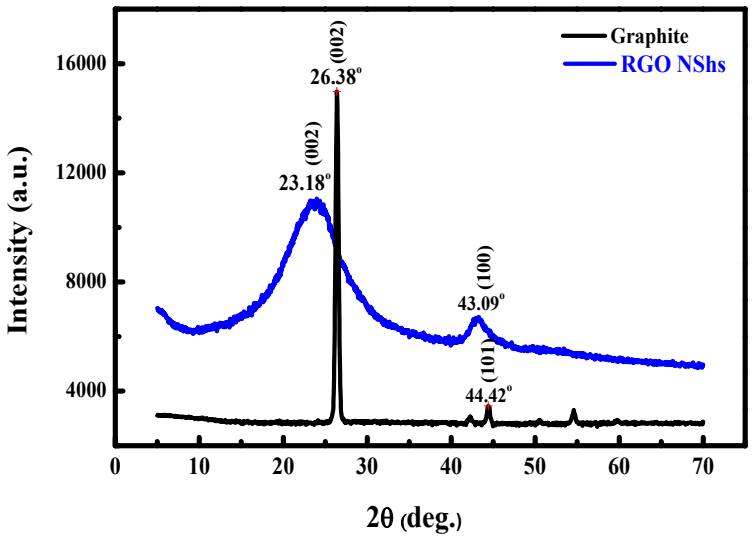

Figure 4. XRD patterns of graphite and RGO NShs.

The interlayer spacing (d) of RGO was estimated using Bragg's law for a hexagonal structure as follows [17,50]:

$$n\lambda = d\sin\theta \qquad \text{and} \qquad \text{hence} \qquad \frac{1}{d^2} = \frac{4}{3}.\frac{h^2+hk+k^2}{a^2} + \frac{l^2}{c^2} \tag{3}$$

where n is the order of diffraction, θ is the diffraction angle, and a and c are the lattice parameters. The interlayer spacing values calculated for the (002) and (001) reflections of RGO were d_{002} = 3.51 ± 0.02 Å and d_{001} = 2.15 ± 0.02 Å, respectively. The average crystallite size (l) was determined from the peak broadening using the Scherrer equation [19,51]:

$$l = \frac{K\lambda}{\beta\cos\Theta} \tag{4}$$

where K = 0.89 is Scherrer's constant, λ is the wavelength of the incident X-ray radiation, and β is the full width at half maximum (FWHM). The noticeable diffraction peak broadening confirms the nanoscale nature of the synthesized RGO. The crystallite sizes calculated for the (002) and (001) planes were l_{002} = 6.84 ± 0.30 nm and l_{001} = 6.84 ± 0.30 nm, respectively. The dislocation density (δ), which reflects lattice imperfections, was estimated using the relation [20,22]:

$$\delta = \frac{1}{l^2} \tag{5}$$

The calculated dislocation densities were δ_{002} = 2.14 ± 0.1 × 10^{14} m^{-2} and δ_{001} = 6.1 × 10^{16} m^{-2} for the (002) and (001) planes, respectively. The microstrain (ε), associated with lattice distortions, was evaluated using the following expression [25,50]:

$$\varepsilon = \frac{\beta}{4\tan\Theta} \tag{6}$$

The microstrain values obtained for the (002) and (001) reflections were ε_{002} = 4.12 ± 0.2 × 10^{-4} and ε_{001} = 2.33 × 10^{-2}, respectively. The lattice parameters corresponding to the hexagonal RGO-like structure were calculated using the relation [27]:

$$C = 2.d \tag{7}$$

Accordingly, the lattice parameters were estimated as C_{002} (c-axis) = 7.02 Å and C_{001} = a = 2.46 Å. The degree of crystallinity (Xc) was evaluated by comparing the integrated area of the crystalline peaks to the total area, including the amorphous contribution, using the following relation [23,27]:

$$X_c = \frac{I_{crystalline} - I_{amorphous}}{I_{crystalline}} \text{ x}100 \tag{8}$$

The calculated crystallinity degrees for the (002) and (001) planes were XC_{002} = 40.1 ± 0.8% and XC_{001} = 38.6 ± 0.5%, respectively. The preferred crystallographic orientation was assessed using the texture coefficient (TC), calculated according to the following equation [36]:

$$TC(hkl) = \frac{I(hkl)/I_o(hkl)}{\frac{1}{N}\sum_{n=1}^{N} I(hkl)/I_o(hkl)} \quad (9)$$

where I(hkl) is the measured intensity of each plane, I_0(hkl) is the corresponding standard intensity from the JCPDS database, and *N* is the number of considered diffraction peaks (N = 2). The calculated texture coefficients were TC_{002} = 1.24 and TC_{001} = 0.76, indicating a preferential orientation along the (002) plane. The structural parameters derived from the XRD analysis of RGO NShs are summarized in Table 1.

Table 1. The calculated XRD parameters of RGO NShs.

Parameter	(002)	(100)
2θ (°)	23.18 ± 0.05	43.09 ± 0.05
d-spacing (Å)	3.51 ± 0.02	2.15 ± 0.02
Crystallite Size, l (nm)	6.84 ± 0.30	~4.0
Microstrain (ε)	4.12 ± 0.2 × 10^{-4}	~2.33 × 10^{-2}
Dislocation Density (δ, m^{-2})	2.14 ± 0.1 × 10^{14}	~6.1 × 10^{16}
Texture Coefficient (TC)	1.24	0.76
Lattice Parameters (Å)	c = 7.02	a = 2.46
Degree of Crystallinity (%)	40.1 ± 0.8	38.6 ± 0.5

3.1.2. XRD of ZnO NPs

The XRD pattern of ZnO NPs exhibits distinct peaks that can be indexed to the hexagonal wurtzite structure, in agreement with the standard JCPDS data for ZnO. Characteristic reflections are located at 2θ values of approximately 31.7°, 34.4°, 36.2°, 47.5°, 56.6°, 62.8°, 66.3°, 67.9°, and 69.1°, corresponding to the (100), (002), (101), (102), (110), (103), (200), (112), and (201) planes, respectively as indicated in Figure 5.

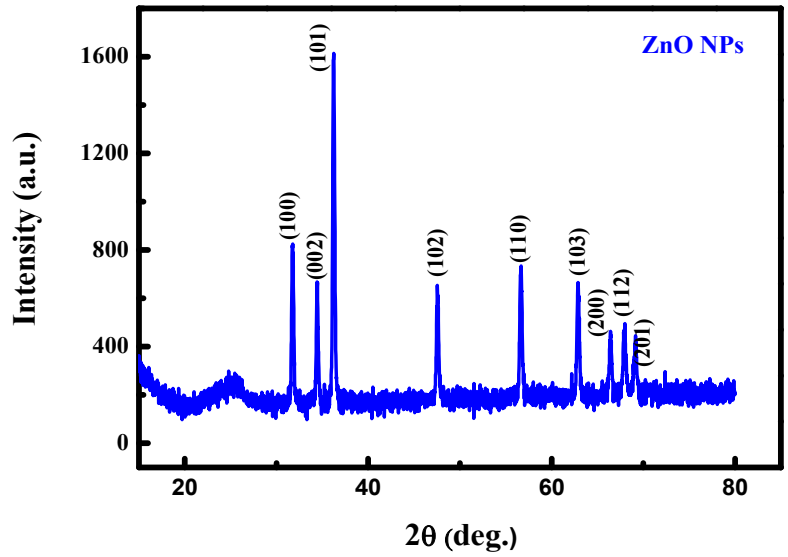

Figure 5. XRD pattern of ZnO NPs.

The sharp and intense diffraction maxima confirm the high crystallinity of the nanoparticles, while the absence of secondary peaks verifies their phase purity. The predominance of the (101) reflection further indicates a preferential growth orientation, a common feature of ZnO nanostructures. These findings collectively demonstrate the successful synthesis of pure, crystalline ZnO with nanoscale dimensions. Table 2 summarizes the structural parameters of ZnO NPs.

Table 2. The calculated XRD parameters of ZnO NPs.

(hkl)	2θ (deg)	d-spacing (Å)	FWHM β (rad)	l (nm)	(ε) x 10^{-3}	(δ) x 10^{-4} (nm^{-2})	TC	χ_c (%)
(100)	31.7	2.81	0.004	37.64	3.37	7.06	0.56	97.2
(002)	34.4	2.60	0.003	44.42	2.63	5.02	0.52	97.2
(101)	36.2	2.48	0.004	38.70	2.88	6.68	0.63	97.2
(102)	47.5	1.91	0.004	37.59	2.29	7.08	1.18	97.2
(110)	56.6	1.62	0.005	35.03	2.08	8.15	0.88	97.2
(103)	62.9	1.48	0.005	36.51	1.82	7.51	0.85	97.2
(200)	66.4	1.40	0.004	38.30	1.65	6.81	1.34	97.2
(112)	68.0	1.38	0.005	36.26	1.71	7.60	1.02	97.2
(201)	69.12	1.36	0.006	37.05	1.65	7.29	2.02	97.2

3.1.3. XRD of ZnO/RGO NCs

The XRD analysis of the ZnO/25% RGO NC reveals distinct diffraction peaks characteristic of the hexagonal wurtzite phase of ZnO. The observed reflections can be indexed to the (100), (002), (101), (102), (110), (103), (200), (112), and (201) crystallographic planes, as shown in Figure 6. The sharpness and intensity of these peaks indicate high crystallinity and well-ordered lattice structures within the nanocomposite. The characteristic peak of RGO is also present, suggesting effective combination of RGO into the ZnO matrix without disrupting the crystallographic orientation of ZnO. No additional impurity peaks were detected, confirmative the phase purity of the produced nanocomposite. The broadening of the diffraction peaks further reveals the nanoscale crystallite dimensions and possible lattice strain effects, which are consistent with the formation of

ZnO NPs embedded in the RGO framework. Table 3 summarizes the structural parameters of ZnO/25%RGO NC [51].

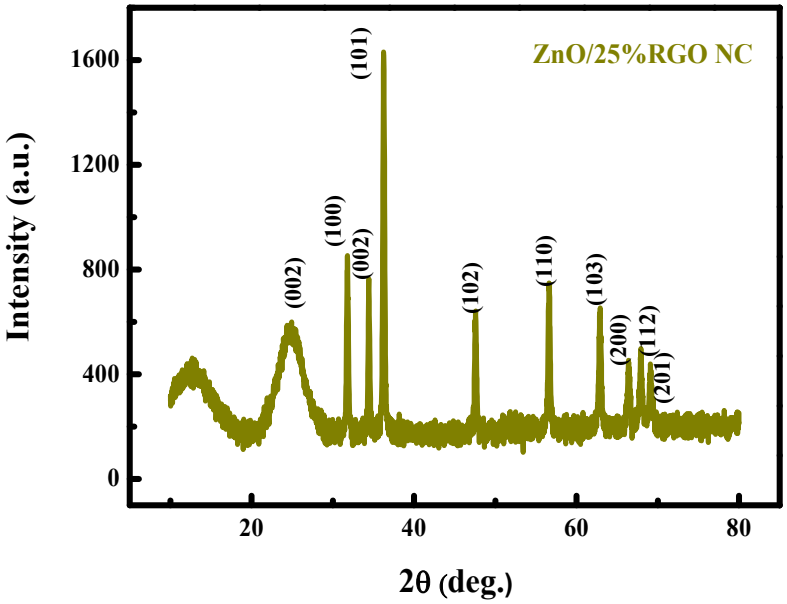

Figure 6. XRD pattern of ZnO/25% RGO NC.

Table 3. The calculated XRD parameters of ZnO/25%RGO NC.

Phase	(hkl)	2θ (deg)	d-spacing (Å)	β (rad)	l (nm)	(ε) x 10^{-3}	δ x 10^{-4} (nm^{-2})	TC	X_c (%)
RGO	(002)								82.8
RGO	(100)								82.8
ZnO	(100)	31.8	2.81	0.004	35.12	3.60	8.12	0.57	82.81
ZnO	(002)	34.4	2.60	0.003	40.13	2.92	6.21	0.58	82.81
ZnO	(101)	36.2	2.48	0.003	36.79	3.02	7.39	0.63	82.82
ZnO	(102)	47.9	1.91	0.004	33.83	2.54	8.75	1.17	82.83
ZnO	(110)	56.8	1.62	0.004	33.85	2.16	8.73	0.90	82.82
ZnO	(103)	62.8	1.48	0.005	31.66	2.09	9.98	0.82	82.82
ZnO	(200)	66.3	1.41	0.005	30.27	2.09	1.09	1.30	82.83
ZnO	(112)	67.9	1.38	0.004	35.87	1.74	7.77	1.03	82.84
ZnO	(201)	69.1	1.38	0.004	35.99	1.69	7.72	2.02	82.85

3.1.4. XRD of ZnO NPs at different RGO concentrations

The XRD patterns reveal the crystalline structures of ZnO/RGO NCs with different RGO loadings. A magnified view of the characteristic diffraction features is presented in Figure 7, where sharp and well-defined peaks confirm the crystalline nature of the ZnO/RGO NCs. The diffraction peaks corresponding to the crystal planes of ZnO, particularly the most intense peak observed at 2θ = 31.8° along with other reflections at higher angles, are indexed to the hexagonal wurtzite structure of ZnO, which is consistent with that reported for typical ZnO-based materials [51]. The lowest diffraction trace (black) represents pure ZnO without RGO incorporation, indicating an unmodified ZnO crystal structure. Notably, the diffraction peak intensities of pure ZnO are lower than those of the ZnO/RGO NCs, suggesting that the incorporation of RGO influences the crystallinity and diffraction behavior of ZnO, while preserving its fundamental wurtzite structure [52].

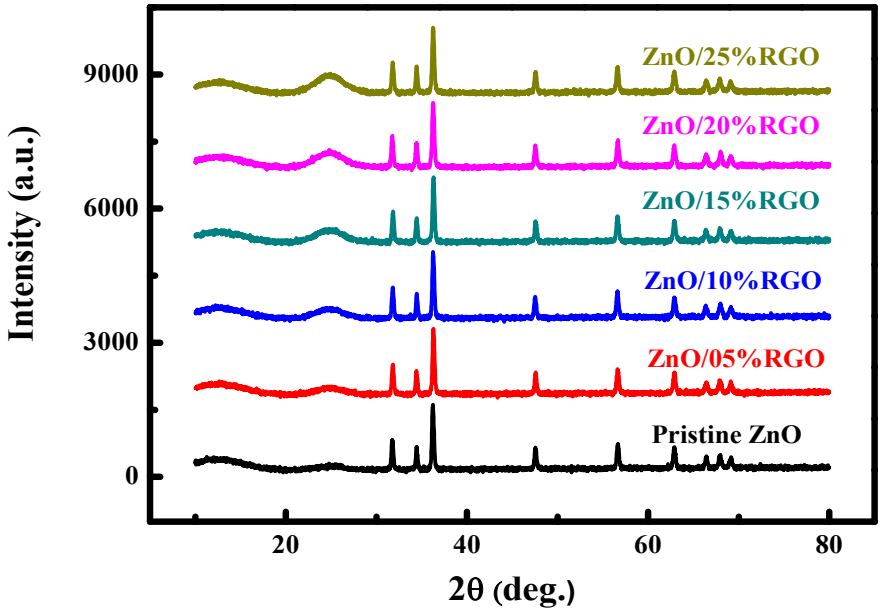

Figure 7. XRD patterns of pristine ZnO NPs and ZnO /RGO NCs at different RGO concentrations.

As the RGO content increases from 5% to 25%, a systematic enhancement in the intensity of all diffraction peaks is observed. This trend indicates that the incorporation of RGO into the ZnO matrix promotes crystallization and/or structural reorganization of ZnO. Concurrently, a gradual broadening of the diffraction peaks is evident with increasing RGO content, suggesting the introduction of lattice strain and/or crystallographic defects arising from the interaction between ZnO and RGO. Moreover, slight shifts in peak positions are observed with varying RGO concentrations, implying subtle changes in the interplanar spacing of ZnO within the crystal lattice. These variations may be attributed to interfacial interactions or local environmental effects within the composite structure. Importantly, such structural modifications do not adversely affect the overall crystallinity or quality of the ZnO/RGO NCs [16,53].

3.2. Morphology and particle size distribution of ZnO, RGO, and ZnO/RGO NCs

Figure 8 illustrates a comprehensive SEM-based analysis of the morphology and particle size distribution of pristine ZnO NPs, RGO NShs, and ZnO/RGO NCs, providing detailed insight into both their structural characteristics and size-related features. As shown in Figure 8 (a), the ZnO sample is composed of quasi-spherical nanoparticles with relatively uniform nanoscale dimensions. A moderate degree of particle agglomeration is observed, which is commonly reported for ZnO nanostructures synthesized via wet-chemical methods. The scale bar of 50 nm confirms that most ZnO NPs possess sizes below 60 nm. The corresponding SEM-derived quantitative morphological parameters for ZnO NPs, RGO NShs, and ZnO/RGO NCs, including particle size and related descriptors, are summarized in Table 4. Figure 8 (b) presents the morphology of RGO NShs, which exhibit thin, layered, and highly wrinkled sheet-like structures with extended lateral dimensions, characteristic of well-exfoliated graphene-based materials. The presence of a clearly defined 100 nm scale bar enables reliable dimensional evaluation and highlights the two-dimensional nature of the RGO NShs. As depicted in Figure 8 (c), ZnO NPs are uniformly and homogeneously anchored onto the surface of the RGO NShs, indicating strong interfacial interactions between ZnO and RGO. Compared with pristine ZnO, a noticeable reduction in nanoparticle agglomeration is observed in the composite, suggesting that RGO effectively serves as a supporting matrix by providing abundant nucleation sites and suppressing particle coalescence. The quantitative particle size distribution derived from SEM image analysis is shown in Figure 8 (d). To ensure statistical

reliability, more than 100 ZnO/RGO particles were measured [51]. The resulting histogram reveals a narrow and slightly asymmetric size distribution, with the majority of particles falling within the 45–55 nm range and an average particle size centered at approximately 50 nm. Only a small proportion of particles exceed 60 nm, indicating limited particle growth and good size uniformity. This well-controlled particle size distribution, together with the intimate interfacial contact between ZnO and RGO, is expected to enhance charge transfer efficiency, increase the availability of active sites, and play a crucial role in the improved sonocatalytic performance of the ZnO/RGO NCs [53].

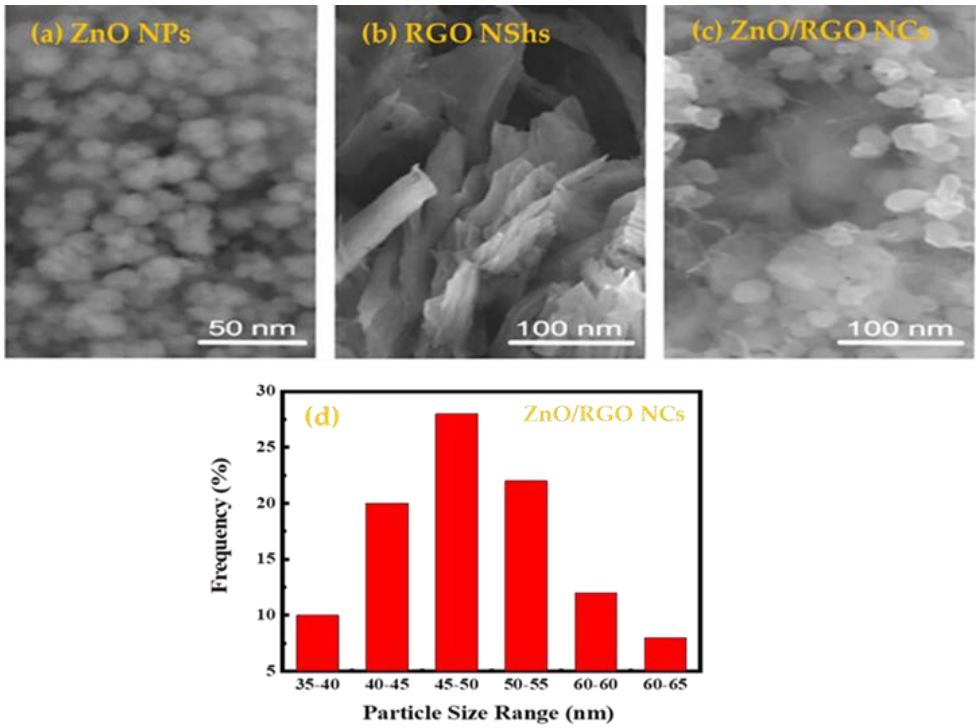

Figure 8. SEM images showing the morphology of **(a)** ZnO NPs, **(b)** RGO NShs, and **(c)** ZnO/RGO NCs, together with **(d)** the corresponding SEM-derived particle size distribution histogram of ZnO/RGO NCs obtained from measurements of more than 100 particles.

Table 4. SEM calculations of ZnO NPs, RGO NShs, and ZnO/RGO NCs.

Material	Structure Type	SEM Scale Bar (nm)	Particle Size (nm)	Feret Diameter (nm)	Projected Area (nm^2)
(a) ZnO NPs	Quasi-spherical NPs	50	25–40	30–45	700–1600
(b) RGO NShs	Wrinkled NShs	100	—	—	—
(c) ZnO/RGO NCs	ZnO NPs incorporated into RGO NShs	100	35–65	40–70	1200–3800

3.3. EDX analysis of ZnO NPs and ZnO/25%RGO NC

Figure 9 (a) presents the EDX spectrum of pure ZnO NPs, whereas Figure 9 (b) shows the EDX spectrum of ZnO/25% RGO NC. In the pure ZnO sample, strong peaks corresponding to Zn and O confirm the successful synthesis of ZnO NPs, with quantitative analysis revealing 79.9 wt% Zn and 20.1 wt% O. After introducing RGO, an additional peak corresponding to carbon (C) emerges in the ZnO/25% RGO NC, with weight percentages of 56.0 wt% Zn, 20.5 wt% O, and 23.5 wt% C. The appearance of carbon peaks verifies the incorporation of RGO sheets into the ZnO matrix, while the

reduced Zn content reflects the partial replacement by the carbonaceous phase. The distinct and well-defined peaks in both spectra highlight the high purity and crystallinity of the synthesized materials, confirming their potential for photocatalytic, sensing, and optoelectronic applications [26,28].

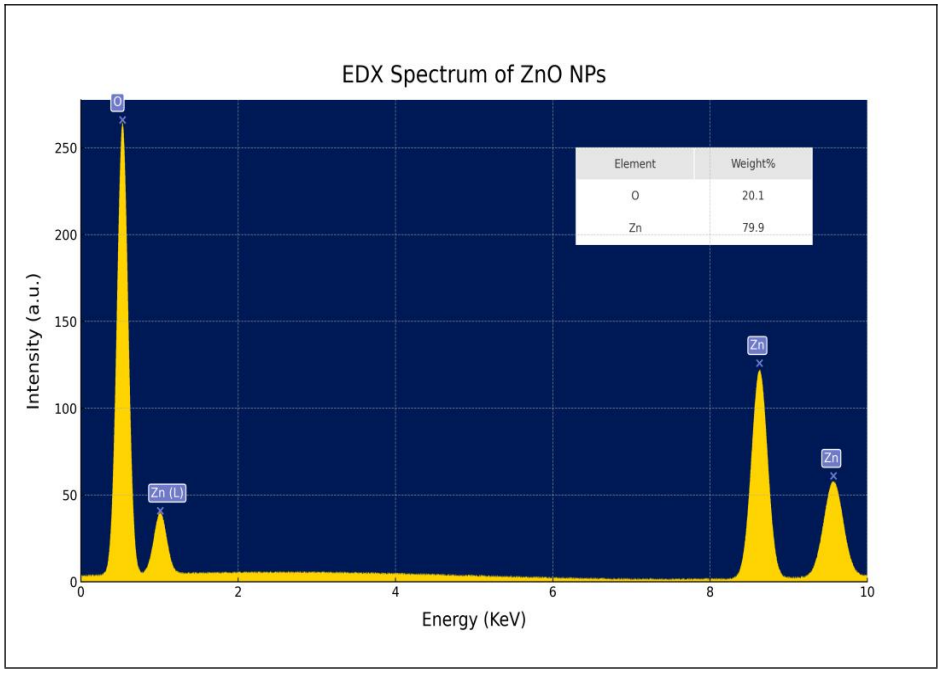

Figure 9 (a). EDX analysis results of ZnO NPs.

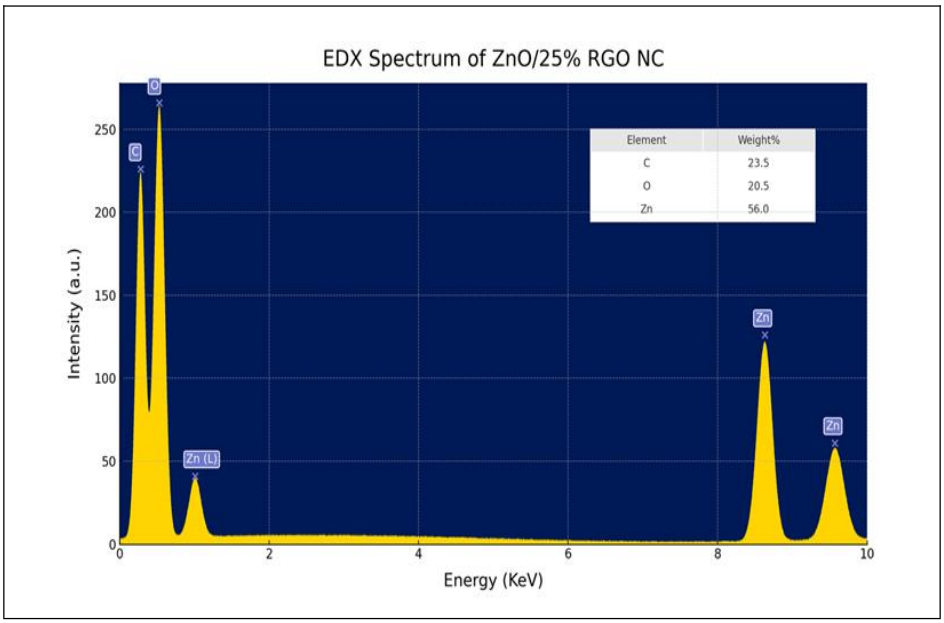

Figure 9 (b). EDX analysis results of ZnO/25% RGO NC.

3.4. FTIR analysis of ZnO NPs and ZnO/RGO NCs

The FTIR spectra of pristine ZnO and ZnO/RGO NCs with varying RGO contents (5–25%) reveal distinct changes in vibrational features that confirm the successful incorporation of RGO into the ZnO matrix [27]. All spectra display a characteristic absorption band below 500 cm^{-1}, assigned to the Zn–O stretching vibration, which verifies the crystalline nature of ZnO. The broad band centered around 3400 cm^{-1} corresponds to O–H stretching vibrations from surface hydroxyl groups and adsorbed water molecules,

and its intensity gradually decreases with increasing RGO content, indicating partial reduction and surface modification as shown in Figure 10.

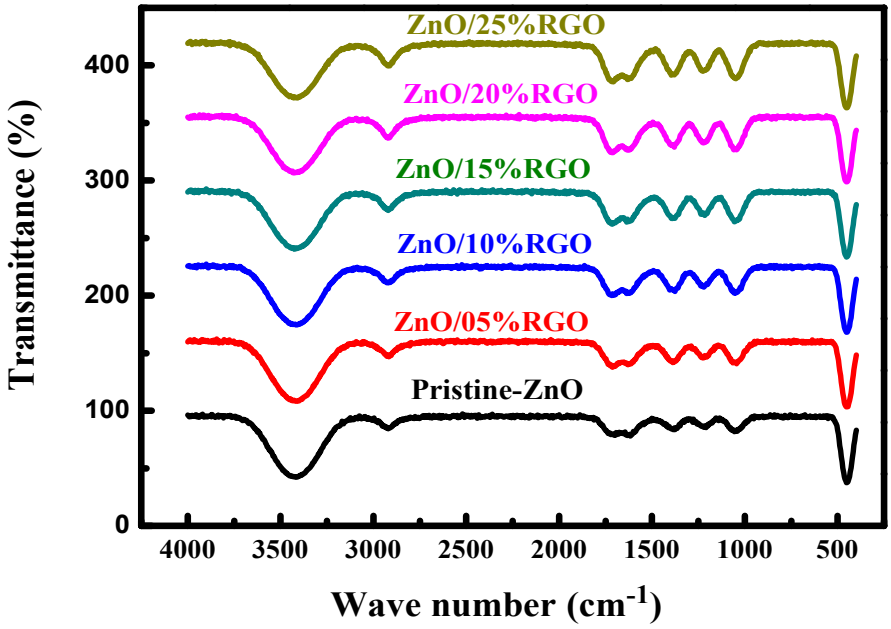

Figure 10. FTIR spectra of pristine ZnO NPs and ZnO/RGO NCs with varying RGO contents.

Additional bands observed near 2920 cm^{-1} (C–H stretching), 1720 cm^{-1} (C=O stretching), 1620 cm^{-1} (C=C and H_2O bending), 1385 cm^{-1} (C–OH bending), 1220 cm^{-1} (epoxy C–O–C), and 1050 cm^{-1} (C–O stretching) become more pronounced with higher RGO loading, reflecting the contribution of oxygenated and graphitic functionalities from RGO. Notably, the progressive enhancement of these carbon-related bands alongside the persistence of the Zn–O peak demonstrates strong interfacial interactions between ZnO and RGO NShs. This spectral evolution highlights the successful hybridization of ZnO with RGO and supports the role of RGO in modifying the surface chemistry, defect structure, and functional group distribution within the composites [29].

3.5. TGA behavior of ZnO/RGO NCs

Figure 11 (a) shows the TGA profile of pure ZnO NPs, while Figure 11 (b) illustrates the thermal behavior of ZnO/RGO NCs with different RGO contents. The ZnO NPs exhibit negligible weight loss, mainly attributed to the evaporation of adsorbed moisture below 150 °C, confirming their high thermal stability [22]. In contrast, the ZnO/RGO NCs display multiple weight-loss stages: the first below 200 °C due to physically adsorbed water and labile oxygen groups, followed by a major loss between 200 °C and 600 °C associated with the decomposition of residual functional groups and partial oxidation of RGO [27]. Notably, the total weight loss decreases as the RGO content increases, indicating improved thermal stability conferred by the RGO framework. These findings demonstrate that the incorporation of RGO enhances the structural integrity and thermal resistance of the nanocomposites at elevated temperatures. TGA calculations of ZnO/RGO NCs using suitable softwares were summarized in table 5.

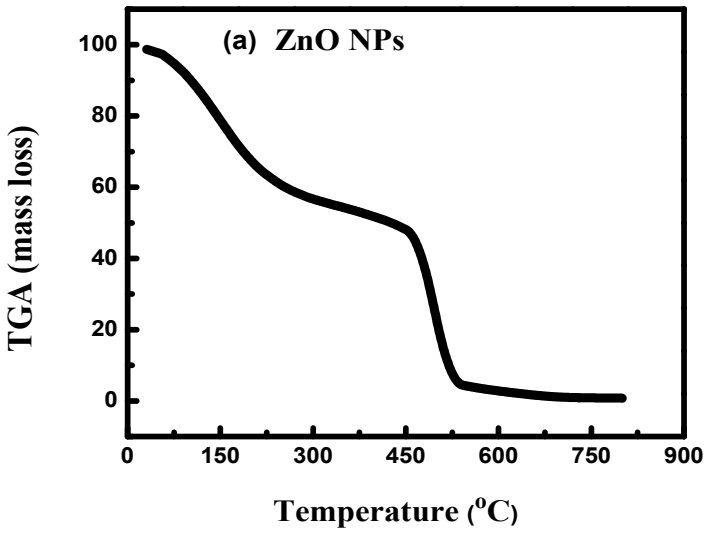

Figure 11 (a). Mass loss versus temperature of ZnO NPs.

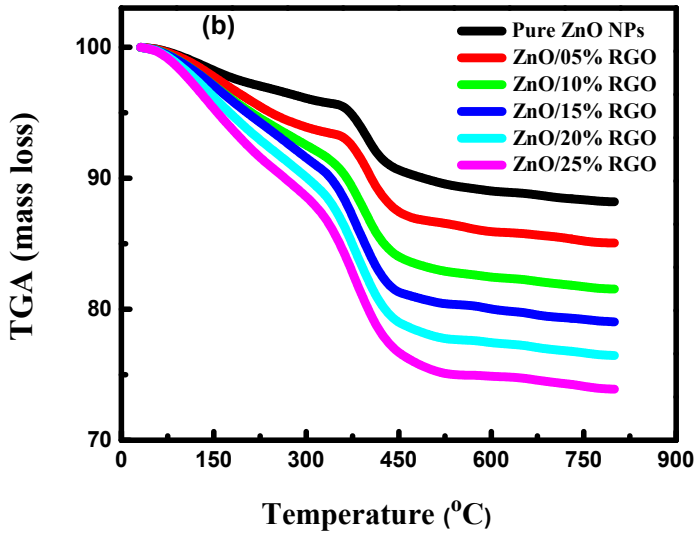

Figure 11 (b). Mass loss versus temperature of ZnO/RGO NCs at different RGO concentrations.

Table 5. Description of TGA curves of ZnO/RGO NCs.

Temperature Range	Event	Weight Loss (%)	Interpretation
30–150°C	Water/solvent loss	3%	Moisture removal
150–400°C	Functional groups decomposition	10%	RGO oxygen groups
400–600°C	RGO backbone combustion	20%	Major RGO loss
600–800°C	Stable	—	ZnO residue remains

3.6. Sonocatalytic performance and stability of ZnO/RGO NCs in MB degradation

This section systematically evaluates the sonocatalytic performance, kinetic behavior, and operational stability of pristine ZnO NPs and ZnO/RGO NCs with different RGO loadings toward MB degradation under ultrasonic irradiation. The analysis integrates degradation profiles, kinetic modeling, removal efficiencies, recyclability, half-life reduction, and initial reaction rates to provide a comprehensive assessment of catalyst performance. All experiments were conducted independently in triplicate (n = 3), and the results are presented as mean ± standard deviation to ensure statistical reliability. Error bars corresponding to standard deviations are included in all relevant figures, and recyclability tests were performed over five consecutive cycles, confirming reproducibility and catalyst durability with relative standard deviations below 5%. The results demonstrate that coupling ultrasonic irradiation with ZnO/RGO heterostructures markedly enhances degradation efficiency compared to pristine ZnO, owing to cavitation-induced charge separation, improved electron transport, and effective suppression of electron–hole recombination. The incorporation of RGO plays a dual role by facilitating interfacial charge transfer and stabilizing ZnO against deactivation during prolonged sonication. Importantly, the catalytic performance depends strongly on RGO loading, with intermediate compositions providing an optimal balance between accessible active sites and charge-carrier mobility [52]. Excessive RGO content, however, can partially shield ZnO surfaces, leading to diminished performance in certain kinetic metrics. Overall, the combined kinetic, stability, and recyclability analyses confirm that rational optimization of RGO loading is critical for achieving high-efficiency and durable ZnO-based sonocatalysts suitable for wastewater treatment applications. These performance enhancements are well explained by the proposed sonocatalytic degradation mechanism (Figure 12), which illustrates the synergistic interaction between ultrasonic cavitation and the ZnO/RGO NCs, leading to intensified charge carrier separation and enhanced generation of reactive oxygen species (•OH and $\bullet O_2^-$) [53].

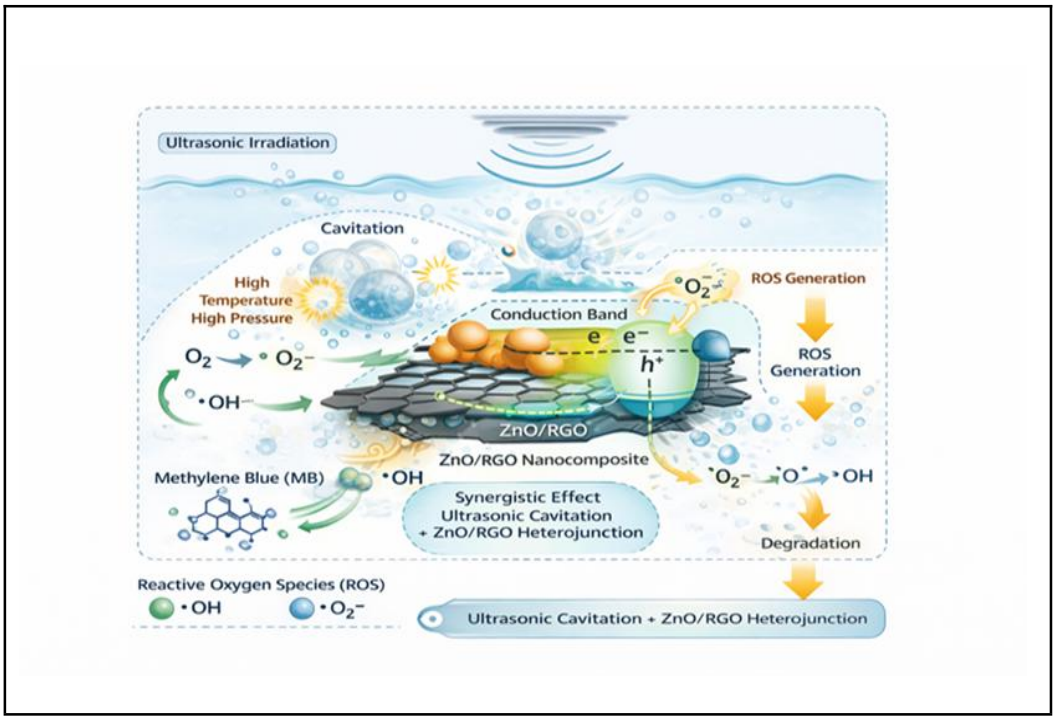

Figure 12. Proposed sonocatalytic degradation mechanism of MB over ZnO/RGO NCs under ultrasonic irradiation, highlighting cavitation-induced charge separation, ROS (•OH, $\bullet O_2^-$) generation, and heterojunction-assisted electron–hole transfer [51–53].

3.6.1. Effect of sonication and catalyst composition on the catalytic degradation of MB

Figure 13 (a) presents the UV–Vis absorption spectra of MB in the absence of sonication using pristine ZnO NPs, monitored over a reaction time of 0–90 min. The characteristic absorption peaks at ~610 and ~665 nm exhibit a gradual decrease in intensity, reflecting a relatively slow degradation process [34,54]. In contrast, Figure 13 (b) shows the spectra obtained under ultrasonic irradiation in the presence of ZnO/25% RGO NC over the same reaction period. A much steeper decline in absorbance is observed, demonstrating an accelerated degradation of MB. The enhanced performance under sonication can be attributed to the combined effects of acoustic cavitation and the improved charge separation efficiency of the ZnO/RGO hybrid system, both of which facilitate faster generation of reactive species. The comparison between the two spectra clearly highlights the superior catalytic efficiency achieved when sonication is coupled with ZnO/25% RGO NCs [33,35].

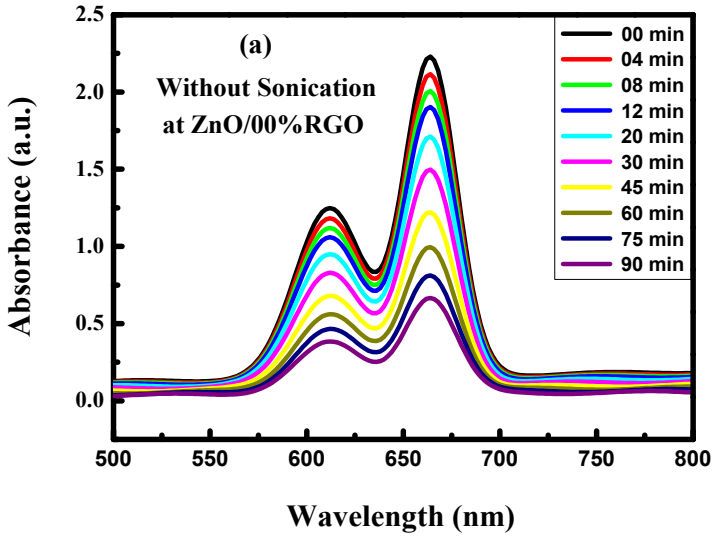

Figure 13 (a). UV–Vis absorption spectra of MB using pristine ZnO NPs without sonication over 0–90 min.

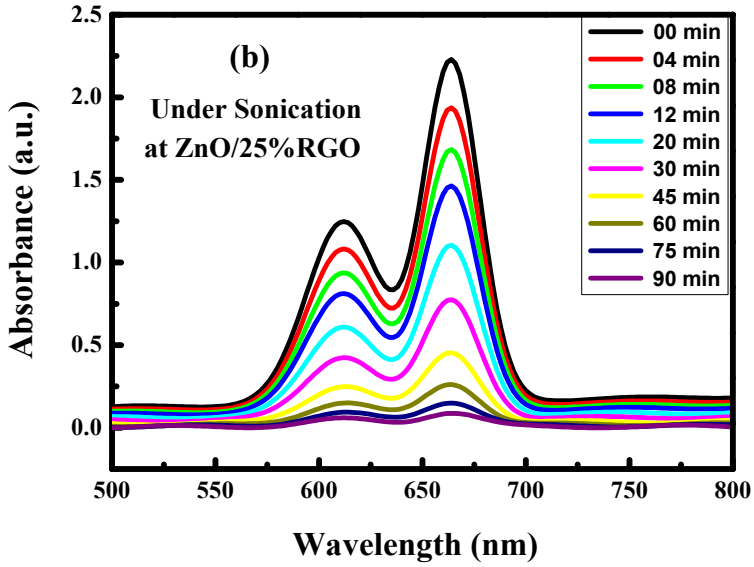

Figure 13 (b). UV–Vis absorption spectra of MB using ZnO/25% RGO NC under sonication over 0–90 min.

3.6.2 Kinetic analysis of sonocatalytic degradation of MB over pristine ZnO NPs and ZnO/RGO NCs

The sonocatalytic degradation behaviors of MB over pristine ZnO NPs and ZnO/RGO NCs with different RGO loadings under ultrasonic irradiation are shown in both Figure 14 (a) and Figure 14 (b) respectively. All degradation experiments were performed in triplicate (n = 3), and the results are reported as mean ± standard deviation to ensure reproducibility and statistical reliability.

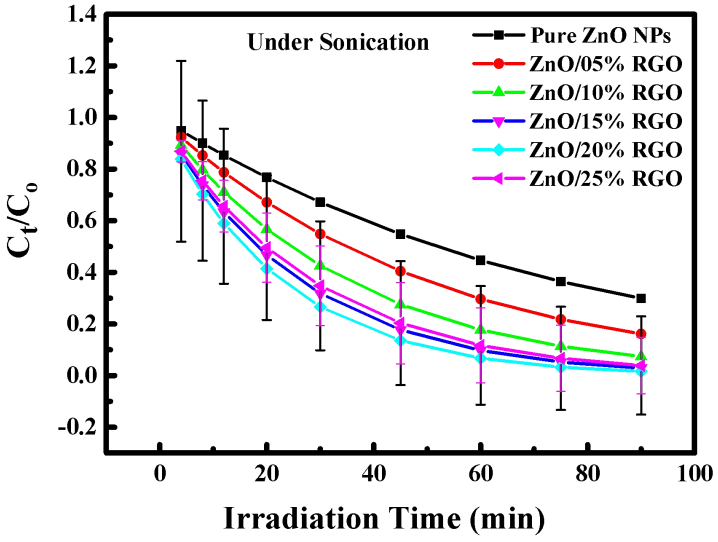

Figure 14 (a). Time-dependent sonocatalytic degradation of MB, expressed as normalized concentration (Ct/Co), under ultrasonic irradiation in the presence of pure ZnO NPs and ZnO/RGO NCs with varying RGO contents (mean ± SD, n = 3).

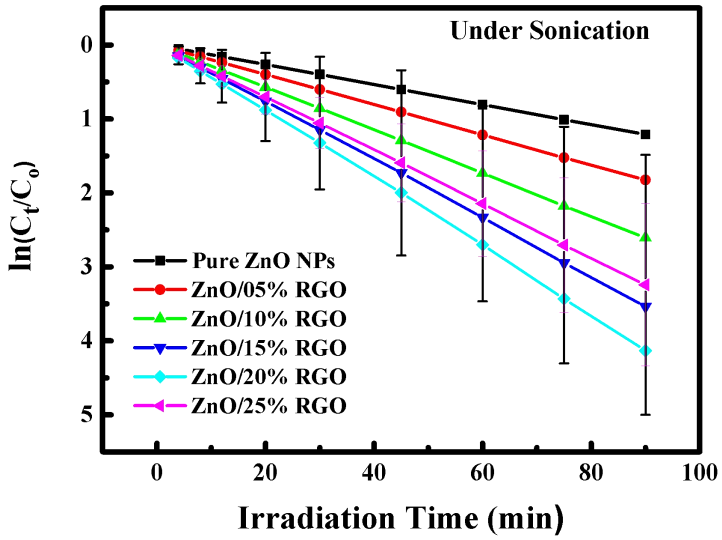

Figure 14 (b). Pseudo–first-order kinetic plots (ln(Ct/Co) versus irradiation time) for the sonocatalytic degradation of MB under ultrasonic irradiation using pure ZnO NPs and ZnO/RGO NCs with different RGO loadings (mean ± SD, n = 3).

As shown in Figure 14 (a), the normalized MB concentration (C_t/C_0) decreases progressively with irradiation time for all samples, while ZnO/RGO NCs exhibit significantly enhanced degradation rates compared to pristine ZnO. Error bars representing standard deviation are included to demonstrate experimental consistency [52,54]. Among the investigated catalysts, the ZnO/25% RGO sample shows the fastest reduction in MB concentration within the examined reaction time (90 minutes), reflecting accelerated degradation kinetics. This enhancement is attributed to the presence of RGO, which promotes efficient interfacial charge transfer, improves adsorption of dye molecules, and facilitates the generation of reactive oxygen species under ultrasonic cavitation.

The pseudo–first-order kinetic plots, shown in Figure 14 (b), exhibit strong linearity, confirming that MB degradation follows pseudo–first-order kinetics under the applied experimental conditions. The apparent rate constants were obtained from linear regression analysis and are reported as mean ± standard deviation. The incorporation of RGO leads to a systematic increase in the kinetic rate constants compared with pristine ZnO, indicating effective suppression of electron–hole recombination and enhanced charge utilization during the sonocatalytic process. In contrast, pristine ZnO exhibits slower reaction kinetics, which is consistent with its limited charge separation efficiency. Furthermore, the inclusion of statistical error bars in Figure 14 (a) and Figure 14 (b) demonstrate the reproducibility and reliability of the observed kinetic trends.

3.6.3. Enhanced sonocatalytic stability and kinetic performance of ZnO/RGO NCs across successive cycles

Figure 15 presents the variation of the apparent kinetic rate constant (K_{eff}) for pristine ZnO NPs and ZnO/RGO NCs with different RGO loadings over five consecutive sonocatalytic cycles. All recyclability experiments were performed in triplicate (n = 3), and the reported kinetic constants are expressed as mean ± standard deviation. Error bars corresponding to standard deviations are included to demonstrate experimental reproducibility and statistical reliability.

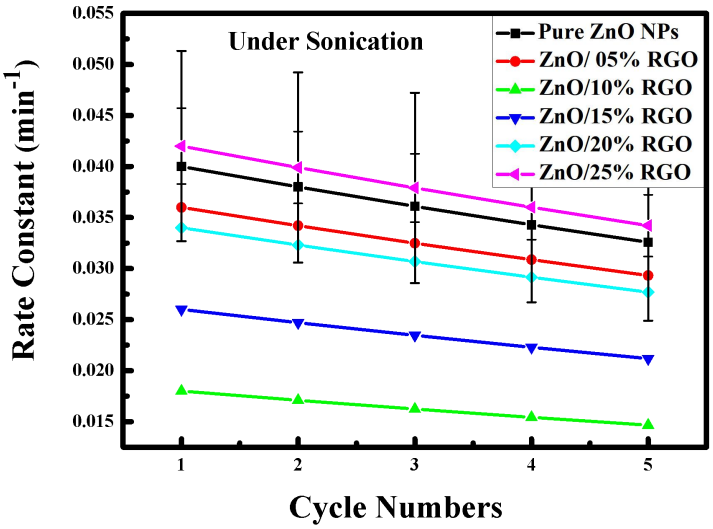

Figure 15. Recyclability performance of pure ZnO NPs and ZnO/RGO NCs with different RGO loadings during repeated sonocatalytic degradation cycles of MB, showing the variation of the apparent rate constant (k) under ultrasonic irradiation (mean ± SD, n = 3)

Pristine ZnO NPs exhibited the lowest K_{eff} values throughout the cycling tests, indicating limited catalytic efficiency and a more pronounced loss of activity upon reuse. In contrast, the incorporation of RGO markedly enhanced both kinetic performance and stability. Among the investigated samples, ZnO/20% RGO NCs consistently displayed the highest K_{eff} across all cycles,

followed by the ZnO/15% RGO sample. Although a gradual decrease in K_{eff} was observed for all catalysts with repeated use, the decline was significantly less pronounced for ZnO/RGO NC compared to pristine ZnO. The relative standard deviations of K_{eff} values remained below 5% across successive cycles, confirming good reproducibility and robust catalytic stability. The improved resistance to deactivation is attributed to the stabilizing role of RGO, which promotes efficient charge separation, facilitates electron transport, and suppresses catalyst degradation under prolonged ultrasonic irradiation [31,35]. These results demonstrate that appropriate optimization of RGO loading is critical for achieving a favorable balance between high sonocatalytic activity and long-term operational stability.

3.6.4 Effect of RGO loading on the sonocatalytic removal efficiency of ZnO/RGO NCs

Figure 16 presents the sonocatalytic removal efficiency of MB at 60 minutes for pristine ZnO and ZnO/RGO NCs with varying RGO loadings. Pristine ZnO achieved only about 50% removal, indicating its relatively low activity. In contrast, the incorporation of RGO markedly enhanced degradation performance, with efficiency progressively increasing as the RGO content increased up to 20%. The ZnO/20% RGO NC achieved the highest efficiency, exceeding 90% within 60 minutes, which can be attributed to the synergistic role of RGO in promoting charge separation and accelerating electron transport [32,34]. However, a slight decline in performance was observed at 25% RGO, likely due to the excessive coverage of ZnO active sites, which limits light absorption and reduces the number of accessible catalytic centers. These findings highlight the importance of optimizing RGO loading, with 20% identified as the most effective balance between charge carrier mobility and surface reactivity for enhanced photocatalytic activity [28,35].

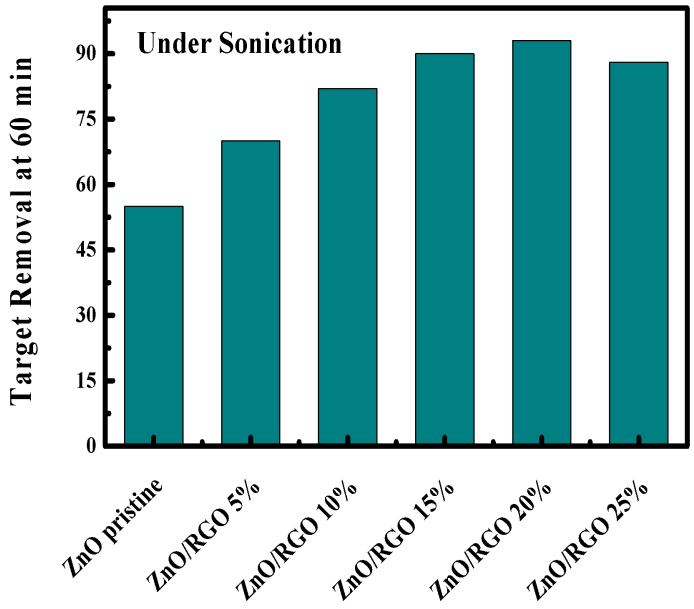

Figure 16. Comparison of MB removal efficiency at 60 min under ultrasonic irradiation using pristine ZnO NPs and ZnO/RGO NCs with different RGO contents, highlighting the effect of catalyst composition on sonocatalytic performance.

3.6.5 Recyclability and stability of ZnO/RGO NCs in sonocatalytic MB degradation

The recyclability and operational stability of pristine ZnO NPs and ZnO/RGO NCs with different RGO loadings during sonocatalytic degradation of MB is shown in both Figure 17 (a) and Figure 17 (b) respectively. Recyclability experiments were performed over five consecutive cycles, with each cycle conducted in triplicate to evaluate statistical reproducibility. As shown in Figure 17

(a), all catalysts exhibit only a marginal decrease in degradation efficiency after repeated use, indicating good structural stability and reusability. Notably, the ZnO/20% RGO NC retains superior performance, maintaining degradation efficiencies above 95% after five cycles, whereas pristine ZnO NPs show a more pronounced decline. The corresponding bar chart in Figure 17 (b) confirms the high reproducibility of the results, with relative standard deviations below 5% across all cycles. This low variability demonstrates the reliability of the recyclability data and confirms the robustness of the catalytic systems. The enhanced durability of the RGO-containing NCs can be attributed to the stabilizing role of RGO, which suppresses ZnO photocorrosion, facilitates efficient charge separation, and preserves active sites during prolonged sonocatalytic operation [30].

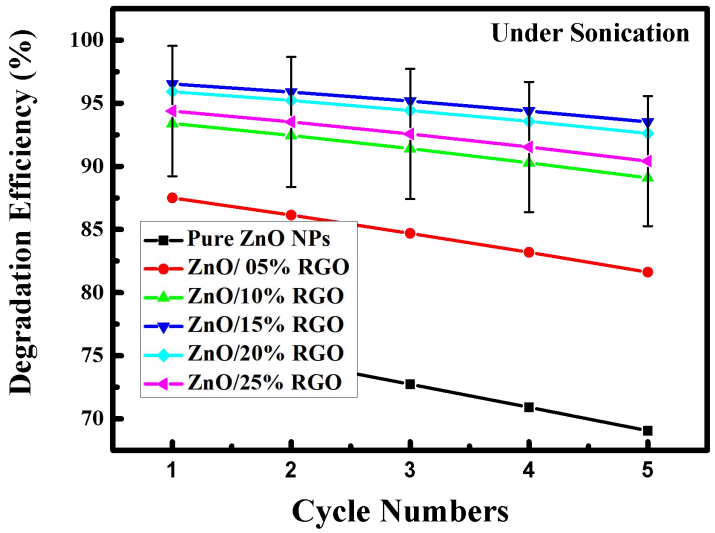

Figure 17 (a). Recyclability performance of pure ZnO NPs and ZnO/RGO NCs with varying RGO contents during sonocatalytic degradation of MB under ultrasonic irradiation over five consecutive cycles (each cycle conducted in triplicate, n = 3; data expressed as mean ± standard deviation).

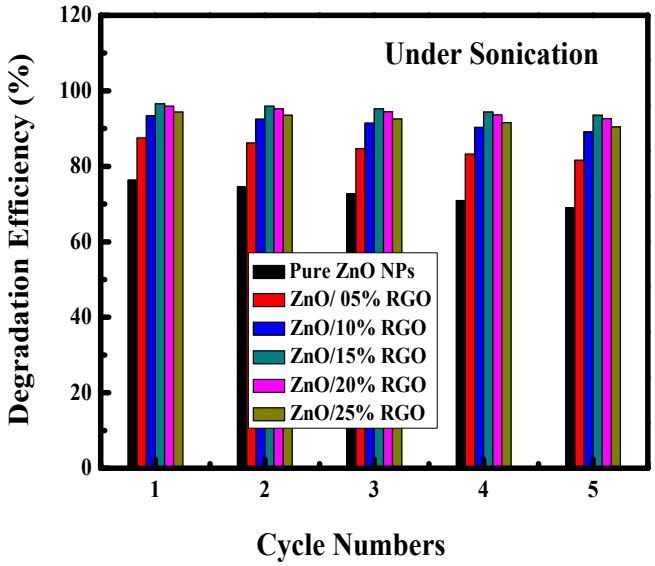

Figure 17 (b). Reusability performance and degradation efficiency of pristine ZnO NPs and ZnO/RGO NCs with different RGO loadings during MB degradation under sonication over five successive cycles.

3.6.6 Stability and reusability of ZnO/RGO NCs under successive sonocatalytic cycles

The retention of the apparent rate constants (K_n/K_1) over five consecutive sonocatalytic cycles was examined (as indicated in Figure 18) to assess the stability and reusability of pristine ZnO and ZnO/RGO NCs. A gradual decline in retention was observed for all samples with increasing cycle numbers, indicating partial deactivation of active sites during repeated use. Pristine ZnO NPs showed the steepest decrease, confirming its poor stability under sonication [55]. In contrast, ZnO/RGO NCs exhibited higher retention, with ZnO/20% RGO NC maintaining about 80% of its initial activity after five cycles. This improved durability is attributed to the presence of RGO, which enhances structural stability, inhibits photocorrosion, and facilitates charge transfer, thereby reducing catalyst deactivation.

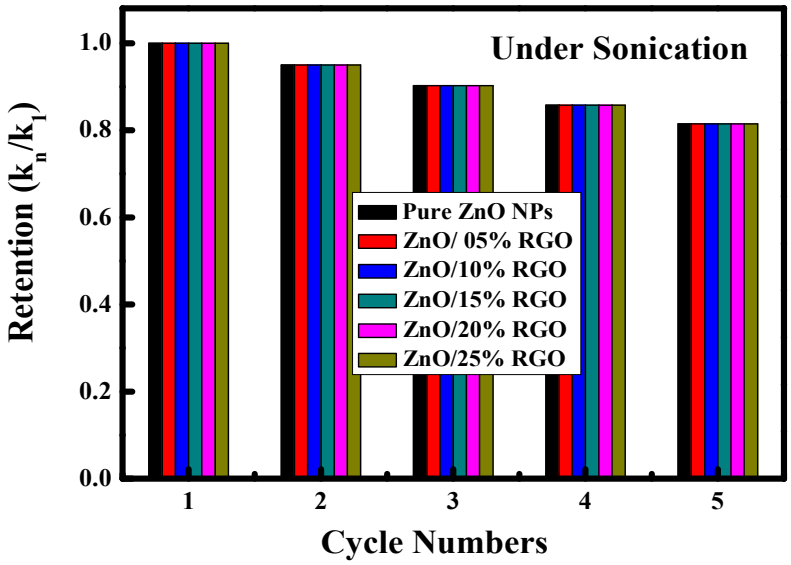

Figure 18. Retention of rate constants (Kn/K1) for Pristine ZnO NPs and ZnO/RGO NCs over five sonocatalytic cycles.

3.6.7 Effect of RGO loading on the half-life of MB degradation under sonication

Figure 19 shows the half-life analysis under sonication and it reveals a significant reduction in degradation time upon incorporating RGO into ZnO nanostructures. Pure ZnO exhibits the longest half-life, indicating relatively slower degradation kinetics. In contrast, ZnO/RGO NCs show a progressive decrease in half-life with increasing RGO content, highlighting the role of RGO in accelerating the catalytic process by facilitating charge separation and minimizing electron-hole recombination. Notably, the ZnO/20% RGO NC achieves the shortest half-life, confirming its superior sonocatalytic activity compared to pristine ZnO and lower RGO loadings. However, a slight increase in half-life is observed at 25% RGO NC, suggesting that excessive RGO may partially shield the active sites of ZnO, thereby reducing catalytic efficiency. These findings demonstrate that the optimized RGO content markedly enhances the catalytic performance of ZnO through improved charge transfer dynamics, thereby advancing its applicability in sonocatalytic degradation processes [53].

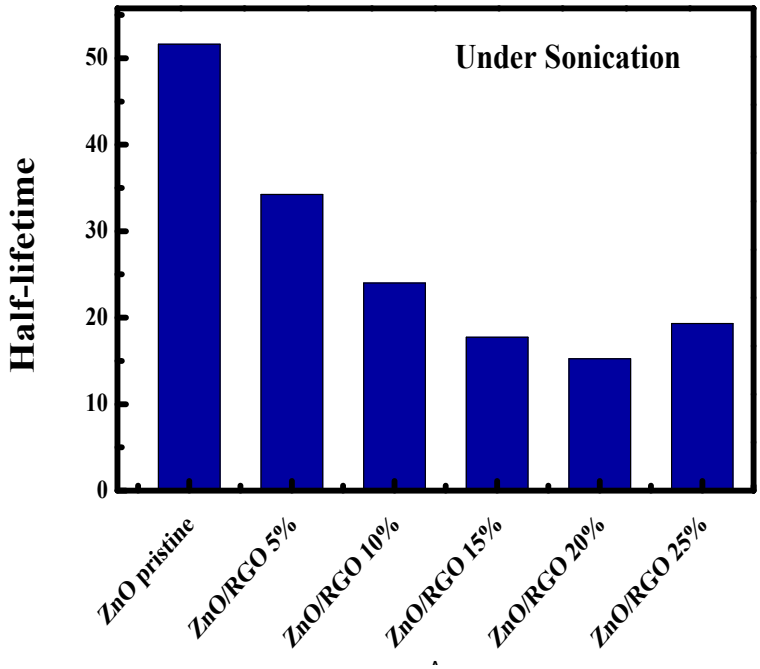

Figure 19. Half-lifetime variations of ZnO NPs and ZnO/RGO NCs during MB degradation under sonication.

3.6.8 Initial reaction rates of ZnO NPs and ZnO/RGO NCs under sonication at different RGO loadings

Figure 20 provides a comprehensive comparison of the initial reaction rates (r_0) of pristine ZnO and ZnO/RGO NCs with different RGO loadings under sonication, expressed using four kinetic representations. In all cases, pristine ZnO shows the lowest reaction rates, confirming its limited intrinsic sonocatalytic activity. As illustrated in panels (a)–(d), the incorporation of RGO markedly enhances the reaction kinetics, with a progressive increase in r_0 observed as the RGO content increases from 5 to 15 wt%. This improvement reflects the strong synergistic interaction between ZnO and RGO, where RGO acts as an efficient electron acceptor and conductive network, promoting rapid charge transfer, suppressing electron–hole recombination, and facilitating the formation of reactive radicals under ultrasonic irradiation. The maximum kinetic performance is consistently achieved at 15 wt% RGO across all kinetic expressions, indicating this composition provides the most favorable balance between interfacial contact and active site availability. Further increasing the RGO content to 20 and 25 wt% leads to a slight reduction in reaction rates, which can be attributed to excessive RGO coverage, particle agglomeration, or partial shielding of ZnO active sites, thereby limiting effective catalytic utilization. Overall, the figure clearly demonstrates that controlled RGO incorporation significantly improves the sonocatalytic kinetics of ZnO, with 15 wt% RGO identified as the optimal loading [51].

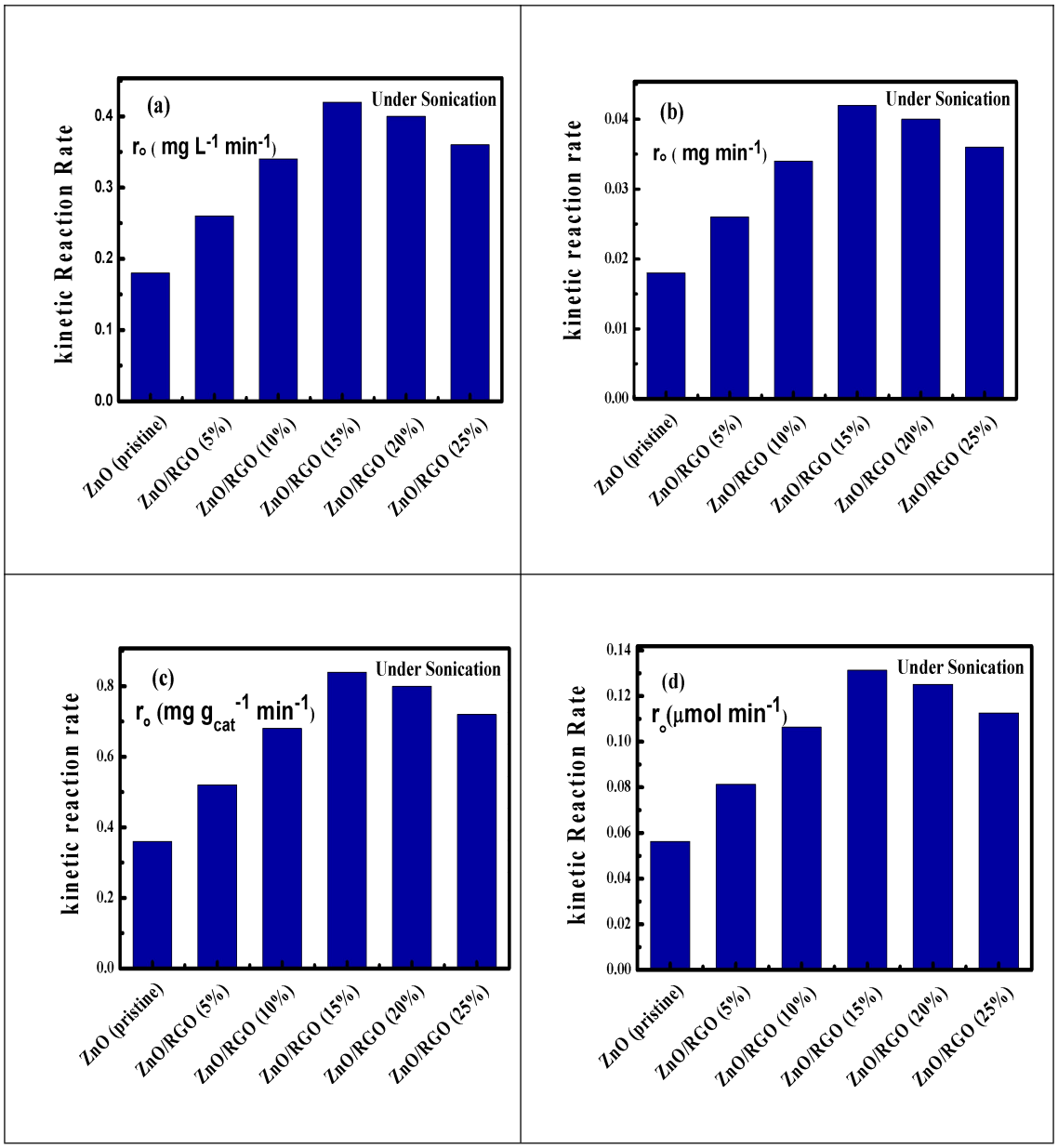

Figure 20. Initial reaction rates of pristine ZnO and ZnO/RGO NCs with varying RGO contents under sonication: **(a)** r_o (mg L^{-1} min^{-1}) is expressed as concentration over time**. (b)** r_o (mg min^{-1}) is expressed as mass over time. **(c)** r_o (mg g_{cat}^{-1} min^{-1}) is normalized to catalyst mass **(d)** r_o (µmol min^{-1}) is expressed in molar units under sonication.

4. Conclusions

In this work, ZnO NPs, electrochemically derived RGO NShs, and a series of ZnO/RGO NCs with systematically varied RGO loadings (5–25 wt%) were successfully synthesized and evaluated for sonocatalytic degradation of MB. Structural and morphological analyses confirmed the formation of highly crystalline wurtzite ZnO with particle sizes predominantly in the range of 30–60 nm, uniformly anchored onto wrinkled RGO NShs, ensuring intimate interfacial contact and effective charge-transfer pathways. Sonocatalytic performance measurements revealed a pronounced enhancement upon RGO incorporation. While pristine ZnO NPs achieved only ~50% MB degradation within 60 min, the optimized ZnO/20% RGO NC exhibited more than 90% degradation under identical ultrasonic conditions. Kinetic analysis demonstrated that MB degradation followed pseudo-first-order behavior, with the apparent rate constant increasing from 0.018 min^{-1} for pure ZnO to a maximum value of 0.051 min^{-1} for ZnO/20% RGO, corresponding to

an approximately threefold enhancement in reaction rate. Consistently, the MB half-life was significantly reduced from 38.5 min (ZnO) to 13.6 min (ZnO/20% RGO), confirming accelerated degradation kinetics. Recyclability and stability assessments further verified the robustness of the ZnO/RGO NCs. The ZnO/20% RGO catalyst retained over 95% of its initial degradation efficiency after five consecutive sonocatalytic cycles, whereas pristine ZnO exhibited a noticeable decline in activity. All kinetic and recyclability experiments were conducted in triplicate, with relative standard deviation (RSD) values below 5%, confirming excellent reproducibility and statistical reliability. The superior sonocatalytic performance of ZnO/RGO NCs is attributed to the synergistic interaction between ultrasonic cavitation and the ZnO/RGO heterointerface, which promotes efficient charge separation, suppresses electron–hole recombination, and enhances reactive oxygen species (•OH and $\bullet O_2^-$) generation. Importantly, excessive RGO loading (≥25 wt%) led to a slight decline in activity, highlighting that 20 wt% RGO represents an optimal balance between interfacial charge transport and accessibility of ZnO active sites. Overall, this study establishes that waste-derived, novel green electrochemically synthesized RGO is an effective and sustainable modifier for ZnO-based sonocatalysts, delivering high degradation efficiency (>90%), fast kinetics ($k = 0.051\ min^{-1}$), and excellent durability (>95% retention). These findings provide clear quantitative evidence supporting the practical potential of ZnO/RGO NCs for wastewater remediation under ultrasonic activation and offer a rational framework for the design of durable, high-performance sonocatalytic systems.

Declarations

Availability of data and material: The datasets used and analyzed during the current study are available from the corresponding author on reasonable request.

Author contributions: **A.M.** conceived and designed the study, conducted the principal experimental work, performed data analysis and interpretation, and prepared the original manuscript. **M.A.I.** and **H.A.Y.** contributed to the experimental work, data analysis, and discussion of the results. **A.A.** contributed to the interpretation of the results and revision of the manuscript. All authors contributed to editorial changes in the manuscript, reviewed the manuscript, and approved the final version of the manuscript. All authors have read and agreed to the published version of the manuscript.

Acknowledgments: The authors acknowledge the Physics Department, Faculty of Science, Suez University, P.O. Box 43221, Suez, Egypt, for providing the facilities and technical support necessary to carry out this research. The authors also gratefully acknowledge E. R. Shaaban for valuable scientific discussions and support.

Funding: This research received no external funding.

Conflicts of interest: The authors declare no conflict of interest.

References

1. Pang Y.L., Tee S.F., Limg S., Abdullah A.Z., Ong H.C., Wu C.H., et al. Enhancement of photocatalytic degradation of organic dyes using ZnO decorated on reduced graphene oxide (rGO). *Desalination and Water Treatment* 2018,108, 311 – 321. https://doi.org/10.5004/dwt.2018.21947
2. Packialakshmi J.S., Albeshr M.F., Alrefaei A.F., Zhang F., Liu X., Selvankumar T., Mythili R. Development of ZnO/SnO ₂ /rGO hybrid nanocomposites for effective photocatalytic degradation of toxic dye pollutants from aquatic ecosystems. *Environmental Research* 2023, 225, 115602. https://doi.org/10.1016/j.envres.2023.115602
3. Negash A., Mohammed S., Weldekirstos H.D., Ambaye A.D., Gashu M. Enhanced photocatalytic degradation of methylene blue dye using eco-friendly synthesized rGO@ZnO nanocomposites. *Scientific Reports* 2023, 13(1), 22234. https://doi.org/10.1038/s41598-023-48826-7
4. Kadhem A.A., Alshamsi H.A. Biosynthesis of Ag – ZnO/rGO nanocomposites mediated by Ceratophyllum demersum L. leaf extract for photocatalytic degradation of Rhodamine B under visible light. *Biomass Conversion and Biorefinery* 2024, 14(19), 24655 – 24669. https://doi.org/10.1007/s13399-023-04501-5

5. Kumar S., Kaushik R.D., Purohit L.P. Heteronanostructured Se–ZnO sustained with RGO nanosheets for enhanced photocatalytic degradation of p-chlorophenol, p-nitrophenol, and methylene blue. *Separation and Purification Technology* 2021, 275(15), 119219. https://doi.org/10.1016/j.seppur.2021.119219
6. Shimizu N., Ogino C., Dadjour M.F., Murata T. Sonocatalytic degradation of methylene blue with TiO_2 pellets in water. *Ultrasonics Sonochemistry* 2007, 14(2), 184–190. https://doi.org/10.1016/j.ultsonch.2006.04.002
7. Elias M., Rahman E., Akter S., Hossain M.A., Jahan R.A., Uddin M.N., Firoz S.H. Eco-friendly fabrication of ZnO–TiO_2–rGO nanocomposite for efficient adsorption-assisted organic dye elimination. *Open Ceramics* 2024, 20, 100691. https://doi.org/10.1016/j.oceram.2024.100691
8. Kousar N., Rasheed S., Yasmeen K., Umar A.R., Laiche M.H., Masood M., et al. Efficient synergistic degradation of Congo red and omeprazole in wastewater using rGO/Ag@ZnO nanocomposite. *Journal of Water Process Engineering* 2024, 58, 104775. https://doi.org/10.1016/j.jwpe.2024.104775
9. Ong C.B., Mohammad A.W., Ng L.Y. Integrated adsorption–solar photocatalytic membrane reactor for degradation of Congo red using Fe-doped ZnO and Fe-doped ZnO/rGO nanocomposites. *Environmental Science and Pollution Research* 2019, 26(33), 33856–33869. https://doi.org/10.1007/s11356-018-2557-2
10. Prabhuraj T., Prabhu S., Dhandapani E., Duraisamy N., Ramesh R., Kumar K.R., Maadeswaran P. Bifunctional ZnO sphere/rGO composites for supercapacitor and photocatalytic activity of organic dye degradation. *Diamond and Related Materials* 2021, 120, 108592. https://doi.org/10.1016/j.diamond.2021.108592
11. Mostafa M.Y., Mostafa A., Abdel-Rahman M., Assem E.E., Ashour A., Badawi E.A. XRD peak broadening modeling for Al-alloy characterization compared with Rietveld profile analysis. *Materials Today: Proceedings* 2023. https://doi.org/10.1016/j.matpr.2023.04.252
12. Mostafa A., Abdel-Rahman M., Mostafa M.Y., Abdel-Rahman M.A., Badawi E.A., Assem E.E., Ashour A. Comparative study of positron and mechanical parameters of cold-worked 3004 aluminum alloy using PALT, PADBT, and HV techniques. *AIP Conference Proceedings* 2023. https://doi.org/10.1063/5.0131866
13. Chaudhary K., Shaheen N., Zulfiqar S., Sarwar M.I., Suleman M., Agboola P.O., Warsi M.F. Binary WO_3–ZnO nanostructures supported on rGO ternary nanocomposites for visible-light-driven photocatalytic degradation of methylene blue. *Synthetic Metals* 2020, 269, 116526. https://doi.org/10.1016/j.synthmet.2020.116526
14. Ramesh K., Gnanavel B., Shkir M. Enhanced visible-light photocatalytic degradation of bisphenol A (BPA) by reduced graphene oxide (RGO)–metal oxide (TiO_2, ZnO, and WO_3) based nanocomposites. *Diamond and Related Materials* 2021, 118, 108514. https://doi.org/10.1016/j.diamond.2021.108514
15. He S., Hou P., Petropoulos E., Feng Y., Yu Y., Xue L., Yang L. Highly efficient visible-light photocatalytic performance of Cu/ZnO/rGO nanocomposite for decomposing of aqueous ammonia and treatment of domestic wastewater. *Frontiers in Chemistry* 2018, 6, 219. https://doi.org/10.3389/fchem.2018.00219
16. Safajou H., Mizwari Z.M., Rostaminia A., Khojasteh H., Aspoukeh P., Mazhari M.P. Green synthesis and enhanced photocatalytic performance of rGO/ZnO/Fe_3O_4 nanocomposites: A sustainable approach to environmental remediation. *Journal of Fluorescence* 2025, 35, 6409–6428. https://doi.org/10.1007/s10895-024-04014-y
17. Hussein S.A., Taha G.M., Adam F.A., Moghazy M.A. Three different methods for ZnO–RGO nanocomposite synthesis and its adsorption capacity for methylene blue dye removal in a comparative study. *BMC Chemistry* 2025, 19, 18. https://doi.org/10.1186/s13065-025-01381-w
18. Fan F., Wang X., Ma Y., Fu K., Yang Y. Enhanced photocatalytic degradation of dye wastewater using ZnO/reduced graphene oxide hybrids. *Fullerenes, Nanotubes and Carbon Nanostructures* 2015, 23(11), 917–921. http://dx.doi.org/10.1080/1536383X.2015.1013187
19. Kaid M.M., Elbanna O., El-Hakam S.A., El-Kaderi H.M., Ibrahim A.A. Effective photocatalytic degradation of organic dyes using ZNC/rGO nanocomposite photocatalyst derived from ZIF-8/rGO thermolysis for water treatment. *Journal of Photochemistry and Photobiology A: Chemistry* 2022, 430, 114001. https://doi.org/10.1016/j.jphotochem.2022.114001
20. Xie M., Zhang D., Wang Y., Zhao Y. Facile fabrication of ZnO nanorods modified with RGO for enhanced photodecomposition of dyes. *Colloids and Surfaces A* 2020, 603, 125247. https://doi.org/10.1016/j.colsurfa.2020.125247

21. Singhal N., Selvaraj S., Sivalingam Y., Venugopal G. Study of photocatalytic degradation efficiency of rGO/ZnO nano-photocatalyst and their performance analysis using scanning Kelvin probe. *Journal of Environmental Chemical Engineering* 2022, 10(2), 107293. https://doi.org/10.1016/j.jece.2022.107293
22. Sharma M., Sondhi H., Krishna R., Srivastava S.K., Rajput P., Nigam S., Joshi M. Assessment of GO/ZnO nanocomposite for solar-assisted photocatalytic degradation of industrial dye and textile effluent. *Environmental Science and Pollution Research* 2020, 27(25), 32076 – 32087. https://doi.org/10.1007/s11356-020-08849-3
23. Al-Zahrani S.A., Khedr A.M., Alturki A.M., El-Yazeed W.S.A. Integration of 2D graphene oxide/zinc oxide nanohybrids for enhancement adsorption and photodegradation of organic pollutants. *Journal of Molecular Liquids* 2024, 395, 123956. https://doi.org/10.1016/j.molliq.2024.123956
24. Kumar S., Kaushik R.D., Purohit L.P. Novel ZnO tetrapod – reduced graphene oxide nanocomposites for enhanced photocatalytic degradation of phenolic compounds and MB dye. *Journal of Molecular Liquids* 2021, 327, 114814. https://doi.org/10.1016/j.molliq.2020.114814
25. Chaudhary K., Aadil M., Zulfiqar S., Ullah S., Haider S., Agboola P.O., Shakir I. Graphene oxide and reduced graphene oxide-supported ZnO nanochips for removal of basic dyes from industrial effluents. *Fullerenes, Nanotubes and Carbon Nanostructures* 2021, 29(11), 915 – 928. https://doi.org/10.1080/1536383X.2021.1917553
26. Zhou M., Yang H., Xian T., Li R.S., Zhang H.M., Wang X.X. Sonocatalytic degradation of Rhodamine B over $LuFeO_3$ particles under ultrasonic irradiation. *Journal of Hazardous Materials* 2015, 289, 149 – 157. http://dx.doi.org/10.1016/j.jhazmat.2015.02.054
27. Nisar A., Saeed M., Muneer M., Usman M., Khan I. Synthesis and characterization of ZnO-decorated reduced graphene oxide (ZnO-rGO) and evaluation of its photocatalytic activity toward photodegradation of methylene blue. *Environmental Science and Pollution Research* 2022, 29(1), 418 – 430. https://doi.org/10.1007/s11356-021-13520-6
28. Hassani A., Khataee A., Karaca S., Karaca C., Gholami P. Sonocatalytic degradation of ciprofloxacin using synthesized TiO_2 nanoparticles on montmorillonite. *Ultrasonics Sonochemistry* 2017, 35, 251 – 262. http://dx.doi.org/10.1016/j.ultsonch.2016.09.027
29. Hassandoost R., Kotb A., Movafagh Z., Esmat M., Guegan R., Endo S., Doustkhah E. Nanoarchitecturing bimetallic manganese – cobaltite spinels for sonocatalytic degradation of oxytetracycline. *Chemical Engineering Journal* 2022, 431, 133851. https://doi.org/10.1016/j.cej.2021.133851
30. Chong S., Zhang G., Wei Z., Zhang N., Huang T., Liu Y. Sonocatalytic degradation of diclofenac with FeCeOx particles in water. *Ultrasonics Sonochemistry* 2017, 34, 418 – 425. http://dx.doi.org/10.1016/j.ultsonch.2016.06.023
31. Liu P., Wu Z., Lee J., Cravotto G. Sonocatalytic degradation of antibiotics over activated carbon in cow milk. *Food Chemistry* 2024, 432, 137168. https://doi.org/10.1016/j.foodchem.2023.137168
32. Yehia F.Z., Badawi A.M., Eshaq G., Dimitry O.I.H. Investigation on the sonocatalytic degradation of nitrobenzene using heterogeneous nanostructured catalysts in absence and presence of surfactant. *Egyptian Journal of Petroleum* 2015, 24(3), 265 – 276. http://dx.doi.org/10.1016/j.ejpe.2015.07.011
33. Jun B.M., Kim Y., Yoon Y., Yea Y., Park C.M. Enhanced sonocatalytic degradation of recalcitrant organic contaminants using magnetically recoverable Ag/Fe-loaded activated biochar composite. *Ceramics International* 2020, 46(14), 22521 – 22531. https://doi.org/10.1016/j.ceramint.2020.06.012
34. Khataee A., Saadi S., Safarpour M., Joo S.W. Sonocatalytic performance of Er-doped ZnO for degradation of a textile dye. *Ultrasonics Sonochemistry* 2015, 27, 379 – 388. http://dx.doi.org/10.1016/j.ultsonch.2015.06.010
35. Noorimotlagh Z., Dehvari M., Mirzaee S.A., Jaafarzadeh N., Martínez S.S., Amarloei A. Efficient sonocatalytic degradation of Orange II dye and real textile wastewater using peroxymonosulfate activated with a novel heterogeneous TiO_2 – FeZn bimetallic nanocatalyst. *Journal of the Iranian Chemical Society* 2023, 20(7), 1589 – 1603. https://doi.org/10.1007/s13738-023-02780-3
36. Yein W.T., Wang Q., Feng X., Li Y., Wu X. Enhancement of photocatalytic performance in sonochemically synthesized ZnO – rGO nanocomposites owing to effective interfacial interaction. *Environmental Chemistry Letters* 2018, 16, 251 – 264. https://doi.org/10.1007/s10311-017-0651-1
37. Dharman R.K., Palanisamy G., Oh T.H. Sonocatalytic degradation of ciprofloxacin and organic pollutants by 1T/2H phase MoS_2 in polyvinylidene fluoride nanocomposite membranes. *Chemosphere* 2022, 308, 136571. https://doi.org/10.1016/j.chemosphere.2022.136571

38. Mohamed M.M., Ghanem M.A., Khairy M., Naguib E., Alotaibi N.H. Zinc oxide-incorporated carbon nanotube or graphene oxide nanohybrids for enhanced sonophotocatalytic degradation of methylene blue dye. Applied Surface Science 2019, 487, 539 – 549. https://doi.org/10.1016/j.apsusc.2019.05.135
39. Ahmed M.A., Mohamed A.A. Advances in ultrasound-assisted synthesis of photocatalysts and sonophotocatalytic processes: A review. iScience 2024, 27(1), 108583. https://doi.org/10.1016/j.isci.2023.108583
40. Machín A., Fontánez K., Duconge J., Cotto M.C., Petrescu F.I., Morant C., Márquez F. Photocatalytic degradation of fluoroquinolone antibiotics using Au@ZnO – rGO – g-C_3N_4 composites. *Catalysts* 2022, 12(2), 166. https://doi.org/10.3390/catal12020166
41. Uma K., Munusamy K., Munirathinam E., Yang T.C.K., Lin J.H., Kannaiyan D. Active synthesis of graphene nanosheet-embedded PbS octahedral nanocubes for prompt sonocatalytic degradation. *Journal of Inorganic and Organometallic Polymers and Materials* 2020, 30(9), 3797 – 3807. https://doi.org/10.1007/s10904-020-01531-8
42. Yousaf M.I., Hameed S., Raza M.A. Synthesis and application of Bi_2WO_6/ZnO/rGO nanorod composites as a latent high-performance supercapacitor electrodes. *Journal of Alloys and Compounds* 2024, 1004, 175834. https://doi.org/10.1016/j.jallcom.2024.175834
43. Chan Y.Y., Pang Y.L., Lim S., Chong W.C., Shuit S.H. Plant-mediated synthesis of silver-doped ZnO nanoparticles with high sonocatalytic activity: Sonocatalytic behavior, kinetic and thermodynamic study. *Environmental Science and Pollution Research* 2024, 31(28), 40495 – 40510. https://doi.org/10.1007/s11356-022-24145-8
44. Gadge S., Tamboli A., Shinde M., Fouad H., Terashima C., Chauhan R., Gosavi S. Sonocatalytic degradation of methylene blue using spindle-shaped cerium oxide nanoparticles. *Journal of Solid State Electrochemistry* 2023, 27(8), 2005 – 2015. https://doi.org/10.1007/s10008-023-05464-3
45. Khitab F., Jan M.R., Shah J. Sonophotocatalytic degradation of aqueous Acid Red 27 and Direct Violet 51 using copper-impregnated Al_2O_3. *Desalination and Water Treatment* 2019, 137, 381 – 394. https://doi.org/10.5004/dwt.2019.23194
46. Zhong L.L., Wang C., Cui X. *Use of mesoporous BiOI microspheres for sonocatalytic degradation of tetracycline hydrochloride.* Ecotoxicology and Environmental Safety 2022, 237, 113547. https://doi.org/10.1016/j.ecoenv.2022.113547
47. Chen X., Li J., Chen F. Photocatalytic degradation of MB by novel and environmental ZnO/Bi_2WO_6 – CC hierarchical heterostructures. *Materials Characterization* 2022, 189, 111961. https://doi.org/10.1016/j.matchar.2022.111961
48. Palanisamy G., Bhosale M., Magdum S.S., Thangarasu S., Oh T.H. Hybridization of polymer-encapsulated MoS_2 – ZnO hybrid nanostructures as organic – inorganic polymer films for sonocatalytic-induced dye degradation. *Polymers* 2024, 16(15), 2213. https://doi.org/10.3390/polym16152213
49. Asli S.A., Taghizadeh M. Sonophotocatalytic degradation of pollutants by ZnO-based catalysts: A review. *ChemistrySelect* 2020, 5(43), 13720 – 13731. https://doi.org/10.1002/slct.202003612
50. Jiang H., Zhang X., Gu W., Feng X., Zhang L., Weng Y. Synthesis of ZnO particles with multi-layer and biomorphic porous microstructures and ZnO/rGO composites and their applications for photocatalysis. *Chemical Physics Letters* 2018, 711, 100 – 106. https://doi.org/10.1016/j.cplett.2018.08.013
51. Wang Y., Li F., Li T. Facile synthesis of BiOI/$BaNbO_3$ composites for rapid sonocatalytic degradation of tetracycline hydrochloride. *Journal of Solid State Chemistry* 2024, 333, 124644. https://doi.org/10.1016/j.jssc.2024.124698
52. Veerabaghu P.P., Ramasamy P., Sathe V., Mahalingam U., Mahalingam A., Sagadevan S. Nano-architected titania/gold@GO nanosheets for sonocatalytic degradation of azo dyes in textile wastewater. *Journal of Alloys and Compounds* 2024, 994, 174690. https://doi.org/10.1016/j.jallcom.2024.174690
53. Farhadi S., Siadatnasab F. $CoFe_2O_4$/CdS nanocomposites: Preparation, characterization, and sonocatalytic degradation of organic dyes. *Chinese Journal of Catalysis* 2016, 37(9), 1487 – 1495. https://doi.org/10.1016/S1872-2067(16)62473-7
54. Mahdavi R., Talesh S.S.A. Enhanced selective photocatalytic and sonocatalytic degradation in mixed dye aqueous solution by ZnO/GO nanocomposites: Response surface methodology. *Materials Chemistry and Physics* 2021, 267, 124581. https://doi.org/10.1016/j.matchemphys.2021.124581

55. Song S., Hao C., Zhang X., Zhang Q., Sun R. Sonocatalytic degradation of methyl orange in aqueous solution using Fe-doped TiO_2 nanoparticles under mechanical agitation. *Open Chemistry* 2018, 16(1), 1283 – 1296. https://doi.org/10.1515/chem-2018-0137